Development of pixel super-resolution scanning transmission X-ray microscopy for material science

Zur Erlangung des akademischen Grades eines
DOKTORS DER INGENIEURWISSENSCHAFTEN (Dr.-Ing.)

von der KIT-Fakultät für Maschinenbau des
Karlsruher Instituts für Technologie (KIT)
angenommene

DISSERTATION

von

M.Sc. Talgat Mamyrbayev

Tag der mündlichen Prüfung:	22. Dezember 2020
Hauptreferent:	Prof. Dr. Jan Gerrit Korvink
Korreferent:	Dr. rer. nat. habil. Simon Zabler

Abstract

Thanks to the development of high-quality X-ray focusing optics during the past decades, synchrotron-based X-ray transmission microscopy techniques enable to study specimens with extremely high spatial resolution. However, on one hand at the expense of the field of view (100 μm x 100 μm) and on the other hand to the detriment of the photon energies range (below 20 keV), which significantly limits the specimens' scope to be investigated, particularly in material science.

In this work, the so-called pixel super-resolution scanning transmission hard X-ray microscopy technique was developed, allowing to enlarge the field of view and drastically reduce the scanning time thanks to sub-pixel specimen scanning through a large number of X-ray probes created by biconcave parabolic shaped refractive multi-lenses. High-resolution images with a spatial resolution corresponding to the X-ray (micro-) nanoprobe size are achieved, even if the pixel size of an imaging detector employed for data acquisition is much larger than that.

Since the technique's key element is X-ray optics, the development and fabrication of one (two)-dimensional X-ray refractive multi-lenses (RMLs) for focusing high energy X-rays (17-35 keV) fabricated by deep X-ray lithography and electroplating technique are presented. The X-ray characterization of these optics and microscopy experiments performed at KARA (Germany), Diamond Light Source (England), and SPring-8 (Japan) synchrotron facilities are provided. Since the height of existing refractive multi-lenses still restricts the field of view (maximum in the mm range), the staircase array of RMLs inclined to the substrate was developed, allowing pixel super-resolution scanning transmission hard X-ray microscopy with a 1.64 cm × 1.64 cm field of view while keeping a 780 ± 40 nm resolution using 35 keV X-rays. The scanning time was only about four minutes. The unique capability of the pixel super-resolution scanning transmission hard X-ray microscopy has been demonstrated by imaging biomedical implant abutments fabricated via selec-

tive laser melting using Ti-6Al-4V. Accordingly, the investigation of extended and thick specimens for material science has been demonstrated.

Kurzfassung

Die Entwicklung hochwertiger fokussierender Röntgenoptiken in den letzten Jahrzehnten hat die Transmissionsmikroskopie mit Röntgenstrahlung aus Synchrotronquellen ermöglicht. Proben lassen sich mit extrem hoher Ortsauflösung untersuchen, allerdings einerseits auf Kosten der Bildfeldgröße (bis zu 100 µm x 100 µm) und andererseits bei eingeschränktem Photonenenergiebereich (unter 20 keV), was den Einsatzbereich insbesondere in den Materialwissenschaften erheblich einschränkt.

In dieser Arbeit für den Bereich harter Röntgenstrahlung (17-35 keV) die so genannte rasternde superpixelauflösende Röntgentransmissionsmikroskopie entwickelt. Sie ermöglicht es, das Bildfeld zu vergrößern und zugleich die Scanzeit drastisch zu reduzieren, indem die Probe mit einem durch refraktive bikonkav-parabolische Multilinsen erzeugten Feld aus Fokuspunkten abgerastert wird. Die hochauflösenden Bilder haben eine räumliche Auflösung, in der Größenordnung der Röntgenfokusdurchmesser, und zwar auch wenn die Pixelgröße des zur Datenerfassung eingesetzten Bilddetektors viel größer ist als die Fokusgröße.

Da das Schlüsselelement der Technik eine Röntgenoptik ist, werden die Entwicklung und Herstellung einer (zwei)-dimensionalen brechenden Multilinse zur Fokussierung hochenergetischer Röntgenstrahlung vorgestellt, die mit Hilfe von Röntgentiefenlithographie und Galvanik hergestellt wurde. Es werden die Röntgencharakterisierung dieser Optiken und Mikroskopieexperimente vorgestellt, die an den Synchrotronquellen KARA (Deutschland), Diamond Light Source (England) und SPring-8 (Japan) durchgeführt wurden. Da die Höhe der herkömmlichen refraktiven Multilinsen das Sichtfeld immer noch einschränkt (bestenfalls im Millimeterbereich), wurde eine Treppenanordnung aus zum Substrat geneigten RMLs entwickelt, die eine pixelsuperauflösende Rasterröntgenmikroskopie mit einem Bildfeld von 1.64 cm × 1.64 cm bei einer Auflösung von 780 ± 40 nm unter Verwendung von 35 keV Röntgenstrahlung ermöglicht. Die Scanzeit betrug nur etwa

vier Minuten. Die einzigartigen Möglichkeiten der rasternden superpixelauflösenden Röntgentransmissionsmikroskopie mit harter Röntgenstrahlung wurde durch die Abbildung eines durch selektives Laserschmelzen aus Ti-6Al-4V hergestellten biomedizinischen Implantat-Abutments demonstriert. So wurde die Untersuchung ausgedehnter und dicker Proben für die Materialwissenschaften demonstriert.

Contents

List of Abbreviations

PSR-STHXM	Pixel Super-Resolution Scanning Transmission Hard X-ray microscopy
FoV	Field of View
TXM	(full-field)Transmission X-ray Microscopy
STXM	Scanning Transmission X-ray Microscopy
LR	Low-Resolution image
HR	High-Resolution image
PSR	Pixel Super-Resolution image
CCD	Charged Coupled Device
FZP	Fresnel Zone Plate
KB	Kirkpatrick-Baez mirror
MLL	Multilayer Laue Lenses
CRL	Compound Refractive lenses
RML(s)	Refractive Multi-Lens(es)
CRMLs	Compound Refractive Multi-Lenses
KARA	Karlsruhe Research Accelerator
PMMA	Polymethylmethacrilate
PGMEA	Propylene Glycol Methyl Ether Acetate
PEB	Post Exposure Bake
KIT	Karlsruhe Institute of Technology
IMT	Institute of Microstructure Technology
LIGA	Lithographie, Galvanik, Abformung
EBL	E-beam Lithography
DXL	Deep X-ray Lithography
SPring-8	synchrotron facility in Japan
1D	one-dimensional
2D	two-dimensional
SEM	Scanning Electron Microscope

SHS	Shack-Hartmann sensor
ESF	Edge Spread Function
LSF	Line Spread Function

Acknowledgment

I want to thank Dr. Jürgen Mohr for giving me the opportunity to work in the field of X-ray optics. I thank you for proofreading and giving feedback for the beamtime proposals, publications, and this dissertation. I appreciate your guidance and constant support.

I would like to thank Prof. Dr. Jan Korvink and Dr. rer. nat. habil. Simon Zabler for taking over the duty of being the referees for this dissertation.

I want to thank Prof. Dr. Atsushi Momose for giving me the opportunity to work in the Exploratory Research for Advanced Technology (ERATO) project. Thanks a lot for your supervision and for sharing the ideas.

I would like to thank the support of the Karlsruhe School of Optics and Photonics (KSOP) and the Karlsruhe House of Young Scientists (KHYS).

Special thanks go to Pascal Meyer, without whom the realization of the optical elements used in this work would not have been possible. I am grateful for introducing me to the deep X-ray LIGA process and sharing your experience.

I want to thank Arndt Last for the fruitful discussions about X-ray lenses and for providing some of them. Also, thanks a lot for your comments and suggestions on this dissertation.

I thank Katsumasa Ikematsu for working together within the ERATO project.

Many thanks go to Microworks GmbH: Joachim Schulz, Konradin Kaiser, Thomas Beckenbach, and Ottó Márcus for the fruitful discussions about the limits of the fabrication process.

I want to thank Alexander Opolka for working together on the development of a 2D compound refractive multi-lenses.

I would like to thank the staff at the Institute of Microstructure Technology: Martin Börner, Danays Kunka, Heike Fornasier, Alexandra Moritz, Birgit Hübner, Samuel Bergdolt, Barbara Mattis, Richard Thelen, Andreas Bacher, Stefan Hengsbach, Markus Guttmann and Patrick Doll for the great help.

I thank our Ph.D. students from X-ray optics group: Tobias Schröter, Abrar Faisal, Elisa Kornemann, Michael Richter, Vitor Vlnieska, Margarita Zakharova, Pouria Zangi and Josephine Gutekunst.

Special thanks to Prof. A. Momose's team: Hidekazu Takano and Yanlin Wu for their help and support during the beamtimes at the SPring-8 synchrotron facility.

I want to thank Prof. Dr. Tilo Baumbach, Angelica Cecilia, Marcus Zuber, Sabine Bremer, Tomas Farago for providing the beamtime and their support at the IMAGE beamline/KARA synchrotron facility.

I appreciate many pleasant conversations and discussions with my friends Alexey Ershov, Sergey Lazarev, Dmitriy Busko, and Dmitriy Karpov.

And last but not least, I want to thank my mother and my wife for their patience and infinite support.

Karlsruhe, 29th of October 2020

Talgat Mamyrbayev

1 Introduction

High-resolution X-ray imaging with a large field of view (FOV) is essential for material science applications [1][2][3]. The advantage of X-ray imaging is the shorter wavelength ranging from 10 nm (soft X-rays) to 0.02 nm (hard X-rays) compared to the visible light, which allows to achieve much smaller spatial resolution. Furthermore, the larger penetration depth of X-rays enables to study relatively thick samples in contrast to electron microscopy [4]. The advent of the synchrotron facilities and their wide availability stimulated the rapid development of the high-resolution X-ray imaging techniques at the micro and nanoscale.

Nowadays, X-ray imaging at the synchrotron facilities with a spatial resolution at the sub-micrometer range is achieved by utilizing the so-called indirect X-ray imaging system. This system consists of a scintillator crystal that converts impinging X-rays into visible light, an optical microscope, and a high resolution (Charge Coupled Device) CCD image sensor [5]. Accordingly, the effective pixel size and a spatial resolution of an indirect imaging system are restricted by the diffraction limit of the optics, the thickness of the scintillator material, and a substrate (on which the scintillator is glued) to about 0.5 μm [6]. Furthermore, the field of view is limited to about 1 mm^2 [7].

The spatial resolution limit has been overcome by synchrotron-based X-ray transmission microscopy techniques using X-ray optics to create magnified and focused X-ray images. Nowadays, X-ray microscopy provides a spatial resolution at the nanometer scale, however, further reducing the field of view down to 10 μm^2 [8]. X-ray transmission microscopes can be classified into shadow projection, full-field transmission X-ray microscope (TXM), and scanning transmission X-ray microscope (STXM)[9][10][11] A shadow projection microscope is based on the projecting of the specimen's magnified image onto the detector plane under cone-beam illumination. The spatial

resolution of this technique is defined by the magnification factor, i.e., the distance between the specimen and a virtual source (in case of using X-ray focusing optics) and the distance between the specimen and the detector. In a typical full-field TXM for soft X-rays, the condenser optics is used to illuminate the specimen and Fresnel zone plate to magnify the image onto the detector [12]. In full-field TXM, the FoV is determined by the size of the focused beam on the sample created by the condenser optics. Recently, in the hard X-ray region, hard X-ray TXM based on refractive CRLs as a condenser and magnifying optics has been realized to study eutectic phase transformations in metallic alloys with the spatial resolution of about 100 nm using 15-17 keV X-rays [13][14]. Scanning transmission X-ray microscope utilizes an optical element that creates a single focused X-ray beam (micro or nanoprobe), and an object is raster-scanned across the incoming beam [15][16]. The transmitted X-ray intensity is measured by a typically integrating detector at each specimen scanning position, and the high-resolution image is reconstructed in a pixel-by-pixel manner. The spatial resolution in STXM is equal to the diffraction-limited spot size. For all three types of microscopes, the highest spatial resolution achieved is below 10 nm, and at the moment, the FoV is up to 100 μm x 100 μm at photon energies below 20 keV restricted by the X-ray optics [17][18].

If the FoV takes precedence of the spatial resolution, the pixel super-resolution (PSR) imaging by using low-resolution detectors can be applied [19][20]. The PSR imaging allows to reconstruct a high-resolution image from multiple sub-pixel shifted low resolution (LR) images [21][22][23][24][25][26][27][28][29][30][31][32]. The sub-pixel shifted LR images can be obtained either by the CCD camera's sub-pixel movement or scanning of the specimen [33]. In X-ray imaging, the scanning of a sample with sub-pixel sized steps in front of the detector is preferable because it allows eliminating field inhomogeneity of the incident X-ray beam by flat-field correction [34]. The first demonstration of this technique was performed by the raster-scanning of a specimen in front of the single-photon counting LAMBDA detector (55 μm pixel size) without the use of optical

elements, the FoV of 14×14 mm^2 and the spatial resolution of 10 µm were reached [35].

In this work, we developed a pixel super-resolution scanning transmission hard X-ray microscopy (PSR-STHXM), which combines the advantages of STXM and PSR imaging. The method utilizes sub-pixel specimen scanning through a large number of identical X-ray microprobes periodically spaced, whereas the period corresponds to the pixel size of a low-resolution pixel detector located behind the specimen. The spatial resolution and FoV are determined by the microprobe size and the number of microprobes, respectively. The scan time is reduced in proportion to the number of microprobes. In this thesis, an array of microprobes is formed by refractive multi-lenses. The space between microprobes needs to be equal to a multiple of the size of one pixel at the detector position, and each microprobe should impinge on the center of each pixel. Besides, the PSR-STHXM is developed for the photon energies in the range of 17-35 keV [36][37][38] since many specimens remain opaque at the photon energies below 17 keV.

Thesis goal

This thesis aims to develop the hard X-ray microscopy technique for photon energies above 17 keV and providing a large field of view in the order of centimeters, sub-µm spatial resolution, and relatively short data acquisition time. For this purpose, many steps are involved in getting from the hypothesis of the PSR-STHXM to the successful realization. As a starting point, the concept of PSR-STHXM has to be developed, including the determination of the theoretical limits of the technique. Next, the new X-ray optics were designed and realized, considering the constraints of the fabrication process, synchrotron beamline, and the imaging detector. After the optical elements' manufacturing, the microscopic analyses need to be done to evaluate the quality of the optics and further fabrication process optimization. After achieving the desired optics, which theoretically predicts the (sub-)µm size of X-ray foci, the design, and implementation of the experimental setup at the beamline, including the optics holders, was performed. Then, the optics' focusing performance has to be analysed at synchrotron facility using mono-

chromatic hard X-rays, which is necessary to determine the scanning step of the specimen. Finally, the proof of concept of the PSR-STHXM could be demonstrated by image data processing and the PSR image reconstruction algorithm's development. By analyzing the experimental results and identifying the limits, further development and fabrication of X-ray optics were needed to improve the spatial resolution, enlarge the FoV, and reduce the scanning time of the PSR-STHXM. To overcome the maximum height limit of X-ray optics fabricated by the deep X-ray lithography and electroplating technique, the new concept of X-ray optics was developed and experimentally proven.

Thesis outline

The thesis is divided into six chapters following the introduction. Chapter 2 gives a theoretical background, starting with a brief description of X-rays and synchrotron sources, the interaction of X-rays with matter, and X-ray refractive optics. In chapter 3, the principle of deep X-ray lithography and electroplating developed at the IMT/KIT is described [39][40]. Following this, the design and fabrication of new X-ray optical elements such as nickel 1D refractive multi-lenses (RML) for 17 keV, 2D polymer compound RMLs for 34 keV, and a staircase-array of inclined RMLs for 35 keV X-rays by deep X-ray lithography and electroplating as well as microscopic investigation of the X-ray optics are described in details. In chapter 4 the results of the examinations of the X-ray optical elements' focusing performance under monochromatic X-ray illumination at the IMAGE beamline/KARA, B16 Diamond Light Source and BL20B2/SPring-8 synchrotron facilities are presented. The pixel super-resolution scanning transmission hard X-ray microscopy with the super-resolution reconstruction is presented in chapter 5. The main parameters of the developed PSR-STHXM: spatial resolution, field of view, and scanning time are evaluated and followed by the measurement of dental implant abutment fabricated by selective laser melting as an application. Chapter 6 summarizes the results and gives an outlook of the future extension of PSR-STHXM to the multi-contrast imaging modality.

2 Theory

This chapter starts with a brief description of X-rays and the X-ray sources, followed by a description of the interaction of X-rays with matter and refractive optical elements.

2.1 X-rays and synchrotron source

Wilhelm Röntgen discovered the X-rays in 1895 [41]. X-rays are electromagnetic waves in the region of an Angstrom (10^{-10}m). The X-ray interaction with matter is strongly dependent on the wavelength and, subsequently, the photon energy. According to wave-particle duality, the wavelength λ can be converted into the photon energy E via the frequency f according to $E = hf = hc/\lambda$, where h is Planck's constant and c is the speed of light. The shorter the wavelength, the higher the photon energy. For material science applications, many specimens are opaque at energies below 15 keV. Therefore, photon energies above 15 keV are required [14].

With the advent of synchrotron radiation facilities in the mid to late 1970s, X-ray microscopy has gained rapid development. Third-generation synchrotron radiation sources accelerate the electrons by forcing them on a circular trajectory and thus producing intense X-ray beams. Synchrotron radiation is tunable over a broad energy range. One of the crucial parameters for X-ray microscopy is the brilliance of synchrotron sources. Compared with the conventional source such as an X-ray tube, the synchrotron source's brilliance is about 10^{12} higher. Brilliance is defined as the number of photons per second in a given bandwidth (0.1%), divided by the source size and the solid angle [42]:

$$Brilliance = \frac{Photons/second}{(mrad)^2(mm^2 source\ area)(0.1\%BW)} \quad (2.1)$$

This work was performed at the following beamlines and synchrotron facilities:

- IMAGE beamline KARA synchrotron facility (Germany);
- beamline (BL) B16 Diamond Light Source (England);
- BL20B2 SPring-8 (Japan).

2.2 X-ray optics for PSR-STHXM

There are three main physical phenomena for focusing X-rays: reflection, diffraction, and refraction. Therefore, nowadays, there are various types of producing a sub μm single line or point focus depending on the X-ray interaction with matter at the photon energies below 20 keV. First, reflective focusing optics are Kirkpatrick-Baez or Wolter-type mirrors. Their advantage is that they are achromatic [43][44][45]. The challenging task is the alignment of two pairs of focusing mirrors to produce a point focus. Second, diffractive focusing optics Fresnel zone plates (FZP), Multilayer zone plates (MZP), and Multilayer Laue lenses (MLLs) [46][47]. The diffractive optics are commonly used as pre-focusing or imaging optics at energies below 20 keV. Finally, refractive focusing optics are compound refractive lenses (CRLs) [48]. They are efficient at energies above 15 keV(up to 100 keV) [49]. Therefore, they were chosen as an optical element in this work.

Since the main idea of the PSR-STHXM is the sub-pixel specimen scanning through the periodically spaced X-ray foci using high photon energies (above 15 keV), the array of CRLs -is required. The period should be equal to the low resolution (LR) detector pixel size. Furthermore, all of the X-ray foci should have identical optical properties, particularly the size of the foci (FWHM) and distance between neighboring foci. The resolution of

PSR-STHXM is defined by the X-ray focus size (FWHM). Consequently, the sub-µm X-ray focus size is desired.

Recently, the array of line foci produced by 1D refractive multi-lenses (RMLs) manufactured by silicon etching for high photon energies (10-60 keV) were demonstrated [50][51]. These RMLs generated an array of 30 X-ray line foci with a length of each foci (limited by the height of RMLs) of about 60 µm. Since the number of X-ray foci determines the FoV of PSR- STHXM in the scanning direction, a much larger number of foci is necessary. Moreover, the height of the RMLs should be much higher. Also, the array of 2D CRMLs, fabricated either by additive manufacturing or by embossing process of polyimide foils using a paraboloid needle, were demonstrated for energies below 15 keV and for an FoV of 1 mm^2 and 6.5 ×6.5 mm^2 [52][53][54][55]. Moreover, produced 2D CRMLs include stitching/shifting errors, influencing the focusing performance (the point foci size is in the range of ten microns). Therefore, within the scope of this thesis, 1D RMLs and 2D CRMLs for higher energies (above 15 keV), (sub) µm foci size with a large area (>1 mm^2) were developed [36][37][38]. Consequently, in the following sections, only the basics of refractive lenses will be described.

2.3 Interaction of X-rays with matter

2.3.1 Complex refractive index

The complex index of refraction is given by [42]:

$$n = 1 - \delta + i\beta \tag{2.2}$$

where δ is the refraction index decrement, which is the positive value of the order 10^{-7} to 10^{-5} in solids for energies in the range of 10 keV to 30 keV. The imaginary part β denotes the absorption, and it is three orders of magni-

tude smaller than δ. Both can be derived by a complex atomic scattering factor f [56]:

$$f = Z + f' + if'', \tag{2.3}$$

$$\delta = \frac{N_a r_e \lambda^2 \rho}{2\pi A}(Z + f'), \tag{2.4}$$

$$\beta = \frac{N_a r_e \lambda^2 \varrho}{2_\pi A} f'', \tag{2.5}$$

where r_e is the classical electron radius, λ is the wavelength, N_a is Avogadro's number, Z is the number of the electrons in the element, ρ is the density of the element, and A is the atomic mass. The Beer-Lambert law describes the absorption [57]:

$$I_1 = I_0 \, exp(-\mu d) \tag{2.6}$$

Here I_1 and I_0 are intensities of attenuated and primary waves respectively, μ is the linear absorption coefficient for the photon energy E, and d is the material thickness. The absorption coefficient μ is related to the absorption dex β:

$$\mu = \frac{4_\pi}{\lambda}\beta \tag{2.7}$$

2.3.2 Refraction of X-rays

For X-rays, matter is optically thinner than vacuum because the refractive index $n = 1 - \delta$ is slightly below one. This result is because the phase velocity of X-rays is larger in the matter, and the beam coming from the vacuum (or air) is refracted away from the surface normal according to the Snell's law [57]:

$$n_1 \sin\theta = n_2 \sin\theta' \tag{2.8}$$

Where θ and θ' are the angles between the surface normal and the incident ray and refracted ray, respectively. The difference in the refraction for visible light and X-rays is presented in Figure 2.1.

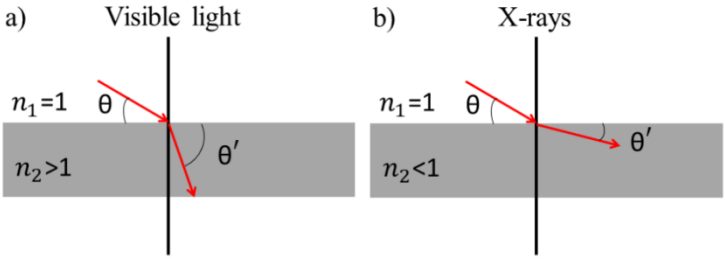

Figure 2.1: Difference in refraction for visible light (a) and for X-rays (b).

Besides, the refraction away from the surface normal implies that the total external reflection occurs when the incident angle is less than the critical angle, which denotes:

$$\theta_c = \sqrt{2\delta} \tag{2.9}$$

Taking into account that δ is in order of 10^{-7} to 10^{-5} the critical angle is in the range of milliradians.

2.4 Refractive X-ray lenses

In contrast to visible light, the low refraction of X-rays made it challenging to fabricate refractive lenses. However, in 1996, the first compound refractive lens (CRL) was experimentally demonstrated [48]. Because the value of δ is very low, the refractive lenses were stacked along the optical axes to achieve a reasonable focal distance. The first CRL consisted of many cylindrical

holes that were drilled in an aluminum block. The large number of holes allowed to obtain the short focal distance in the energy range of 5-40 keV. This CRL generated a focus with strong spherical aberrations caused by the circular profile of the holes.

Over time, the lens profile changed from cylindric to parabolic to avoid spherical aberrations. Therefore, all refractive lenses in this thesis have a biconcave parabolic shape. The parabolic profile is defined as [58][59]:

$$l = \frac{1}{2R} \cdot \left(\frac{A_{\mathrm{ph}}}{2}\right)^2, \tag{2.10}$$

where R is a radius of curvature in the apex of the parabola of the refracting surface.

Consequently, the length of a single refractive lens is equal to:

$$L = 2l + w = \frac{1}{R} \cdot \left(\frac{A_{\mathrm{ph}}}{2}\right)^2 + w, \tag{2.11}$$

Where w is the web distance (distance between two parabola apexes) and A_{ph} is the physical aperture.

The parameters of the single-lens and the X-ray beam refraction (in red) are illustrated in Figure 2.2.

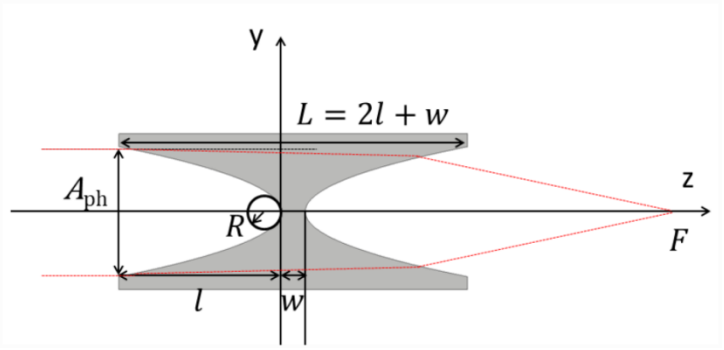

Figure 2.2: The schematic view of a single parabolic X-ray lens with parameters.

The material for CRL manufacturing has a significant influence on the focusing performance of the refractive lenses. Consequently, the best material should have a high refraction power δ, with the lowest possible absorption through a small β. Therefore, the typical lens materials with low absorption (low atomic number) are more suitable for lens fabrication. Nowadays, refractive lenses are made of lithium [60][61], beryllium [62][63][64], silicon [65][66], SU-8 [67][68], diamond [69][70], aluminum and nickel [71][72]; In the context of this thesis, 1D RMLs are made of nickel and 2D CRMLs are made of SU-8 because these materials can be structured by deep X-ray lithography and electroplating. Due to weak refraction of SU-8 lenses at 34 keV, 2D CRMLs consist of many biconcave parabolic shaped lens elements.

Nowadays, the X-ray refractive lenses are widely used at the synchrotron facilities due to their easy alignment, relative insensitivity to misorientations, and mechanical vibrations as focusing and imaging lenses [73]. Since the RMLs consist of identical individual lenses, in the following the main parameters of the single refractive lens for PSR-STHXM are described.

2.4.1 Focal distance

In the PSR-STHXM, the specimen is placed at the focal distance. The focal length of a single biconcave lens is [73]:

$$F = \frac{R}{2\delta} \tag{2.12}$$

R is the radius of curvature of the lens's parabolic shape, and F is its focal length. For a single refractive lens, to obtain a focal distance below 1 m, the radius of curvature should be in the sub-μm range, since δ is small.

For CRLs with large length L, the focal length of a CRL consisting of N single biconcave lens is given by [74]:

$$F = \frac{R}{2\mathrm{N}\delta} + \frac{L}{6} \tag{2.13}$$

Since δ is proportional to $1/E^2$, the focal length varies as the square of the energy, i.e. X-ray lenses are highly chromatic. Therefore, the experiments in this work were performed by using monochromatic X-rays.

2.4.2 Transmission and the effective aperture

Compared to visible light, X-ray lenses are limited by the absorption and the geometrical size (physical aperture A_{ph}) [75]. The absorption limited aperture, which is called effective aperture, is smaller than the physical aperture because the material absorbs the part of the X-ray beam transmitted through the lens (as shown in Figure 2.2).

For the thin lens approximation, the effective aperture is defined by [58]:

$$A_{\mathrm{eff}=A_{\mathrm{ph}}}\sqrt{\frac{1-\exp(-a_{\mathrm{p}})}{a_{\mathrm{p}}}} \tag{2.14}$$

The transmission of an X-ray lens T is the fraction of photons that are transmitted through the lens. The transmission can be derived by integrating Beer-Lambert's law over the lens aperture [58]:

$$T=\frac{\exp(-\mu N w)}{2a_{\mathrm{p}}}\left(1-\exp\left(-2a_{\mathrm{p}}\right)\right) \tag{2.15}$$

where w is the web distance which is the minimal thickness between parabola apexes. a_{p} is the factor responsible for lens material absorption and for scattering on roughnesses of lenses surfaces [58]. For the refractive lenses fabricated by deep X-ray lithography and electroplating, the surface roughness is in the range of 20 nm and therefore can be neglected.

Since a_p is small, the effective aperture can be rewritten as [76]:

$$A_{\mathrm{eff}}=2\sqrt{\frac{F\delta}{\mu}} \tag{2.16}$$

Where μ is the linear absorption coefficient.

The numerical aperture *NA* is related to the effective aperture according to [77]:

$$NA \approx \frac{A_{\text{eff}}}{F} \tag{2.17}$$

2.4.3 Depth of focus and depth of field

Since the specimen is positioned in the focal distance, it is necessary to estimate the longitudinal extension of the focus-the depth of focus (DOF). DOF is determined by twice the length of the region along the optical axis where the diffraction-limited spot diameter Δ_{diff} is equal to the geometrical diameter of a cone extending from the lens's effective aperture to the focus (Figure 2.3) [73]:

$$\text{DOF} = \frac{2F}{A_{\text{eff}}} \cdot \Delta_{\text{diff}} = \frac{2\lambda F^2}{A_{\text{eff}}^2} = \frac{\lambda R^2}{2\delta^2 A_{\text{eff}}^2} \tag{2.18}$$

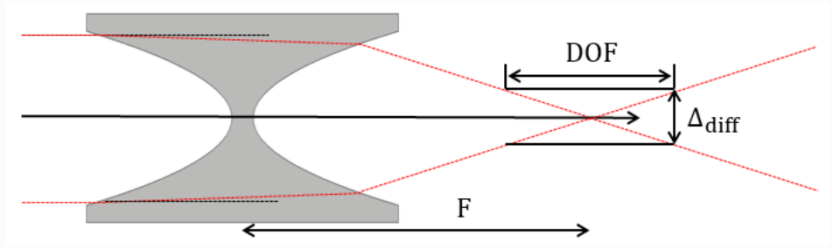

Figure 2.3: The DOF and the size of X-ray foci Δ_{diff}

The depth of field of the refractive lens is defined as the distance along the optical axes between two objects, which can be correctly imaged and can be described by [73]:

$$d_{\text{l}} = \frac{8}{\pi}\frac{\lambda F^2}{A_{\text{eff}}^2}, \tag{2.19}$$

2.4.4 Resolution

The minimum achievable diffraction-limited focus size generated by an X-ray focusing refractive lens is essential because it determines the attainable spatial resolution of the PSR-STHXM. The diffraction-limited spot size Δ_{diff} of the RML, is defined by the effective aperture as [77]:

$$\Delta_{\mathrm{diff}} = \frac{\lambda F}{A_{\mathrm{eff}}} = \frac{\lambda R}{2\delta\, A_{\mathrm{eff}}}, \tag{2.20}$$

3 Microfabrication of X-ray optical elements by deep X-ray LIGA

To realize a PSR-STHXM optical structures with thickness varying from 100 μm to 2 mm and high aspect ratio, high accuracy, and structure details in the sub μm range should be fabricated. The deep X-ray LIGA process, a German acronym for Lithography (Lithographie), Electroplating (Galvanoformung), and Molding (Abformung), meets all these requirements; thus, all optical elements were fabricated using this technique.

3.1 Deep X-ray LIGA process: the basics

The LIGA process [40] is a sequence of microfabrication steps combining a step of deep X-ray lithography (DXRL), also called by some authors deep etch X-ray lithography, and subsequent additive processing of plating-through-mask and molding [39]. In the following, the molding step will not be described as it is not used for the fabrication of the optical component. The deep X-ray lithography is described in Figure 3.1.

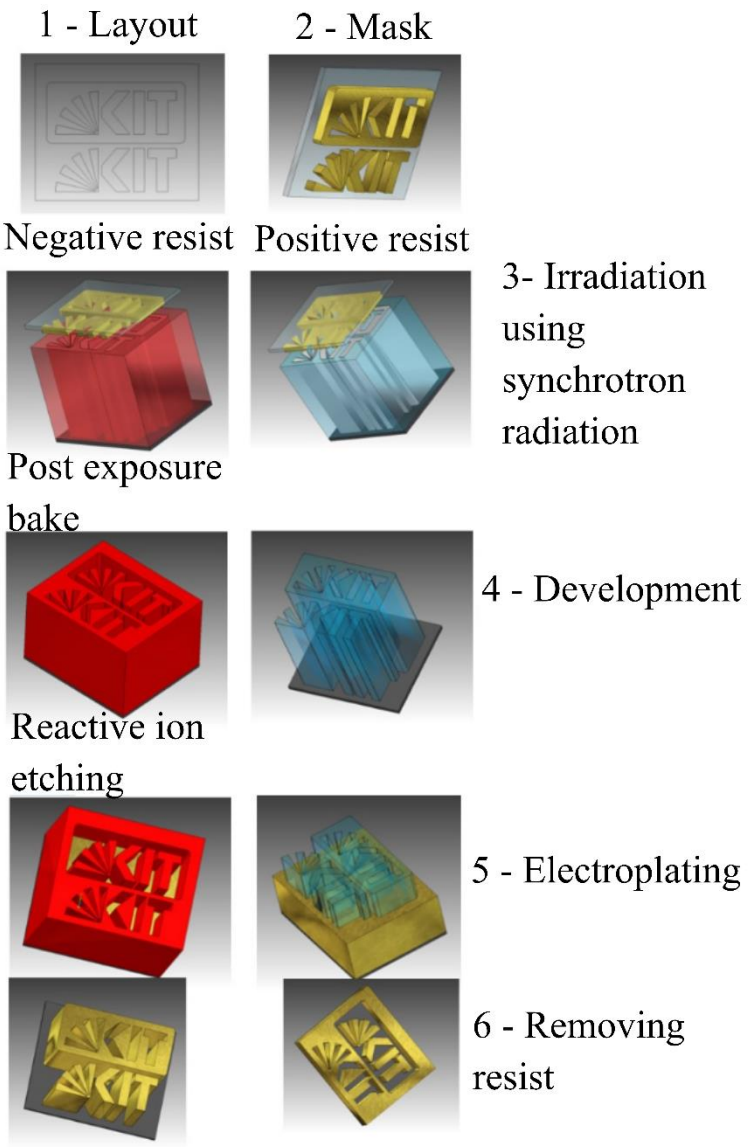

Figure 3.1: The deep X-ray LIG(A) process steps [39]

In the first fabrication step, an X-ray sensitive polymer (resist) layer of up to several millimeters thickness is coated onto a conductive or non-conductive substrate. Generally, polymethylmethacrylate (PMMA) is used as a positive resist and an epoxy-based resist (SU-8) as a negative resist. A mask pattern is transferred into the thick resist layer via a 1:1 shadow proximity printing scheme using hard X-rays from a synchrotron source. X-ray masks consist of absorber patterns (gold) supported by highly X-ray transparent membranes. After irradiation, selective dissolution of the chemically modified exposed parts of the positive resist (or dissolution of the non-exposed regions of the negative resist) in a chemical developer results in a polymeric relief replica of the mask pattern. Then, depending on the material, accuracy, different fabrication routes can be chosen, which may include further steps of electroplating of metal structures [78][79][80][81]. The polymeric microstructure can be used:

- simply as it is (2D compound RMLs) [82],
- as an electroplating template to generate metallic microparts (1D RMLs, and staircase-array of 1D inclined RMLs).

Features characterizing this process are listed below:

- The high-energy X-rays can deeply penetrate thick (e.g., hundreds of micrometers or even millimeters) layers of polymeric resist, allowing uniform deposition of energy in the depth of the resist and the formation of tall microstructures in one exposure step.
- The exact shape-definition of parts, both laterally in terms of dimensional control and in terms of the straightness and planarity of sidewalls, are available.
- The short wavelengths of X-ray photons provide high resolution for patterning due to low diffraction effects. The smallest lateral dimension of a few micrometers with structural details in the sub-micrometer range can be manufactured.

- The X-ray beam's small vertical angular divergence achieves high accuracy in pattern transfer from the mask. Due to their excellent collimation, the X-rays penetrate thick resists with an extremely low horizontal run-out (in the range of 0.1 µm/100 µm thickness), thereby producing the substantially vertical walls for which LIGA structures are well known.
- The vertical sidewalls are optically smooth with a typical local roughness of the order of 10 nm and longer-range waviness, such as slope errors or steps determined solely by the accuracy of mask writing.
- The almost parallel (well collimated) light of X-ray beams produced by synchrotron radiation sources also allows printing with large depth-of-field. A large working distance between the mask and the substrate can then be used in non-traditional pattern transfer to manufacture inclined structures or pattern formation on substrates presenting a large topography.

3.2 Deep X-ray LIGA process at IMT/KIT

IMT has two exposure beamlines at the KARA synchrotron, namely LITHO1 and LITHO2. The two beamlines are equipped with scanners from the company Jenoptik AG (Jena, Germany). The characteristics of the beamlines are indicated in Table 3-1.

For X-ray mask fabrication different processes exist at IMT [39]. Since the optical element should be fabricated with high accuracy, the higher quality mask manufacturing process was chosen (see Figure 3.2); the intermediate mask using a 2.5 µm titanium membrane is processed using an E-beam writer, and the working mask is fabricated using X-ray lithography.

Table 3-1: Characteristics of the X-ray LIGA beamline @ IMT/KIT

Beamline	Characteristics	Energy range (keV)	Min. Au absorber thickness (µm)	Resist height (µm)
LITHO1	Mask fabrica-tion, patterning of thin micro-structures	2.2 - 3.3	0.75-2.2 (Intermediate mask)	Up to 100
LITHO2	Deep X-ray lithography	2.5 - 12.4	20-25 (Working mask)	100 to 2000

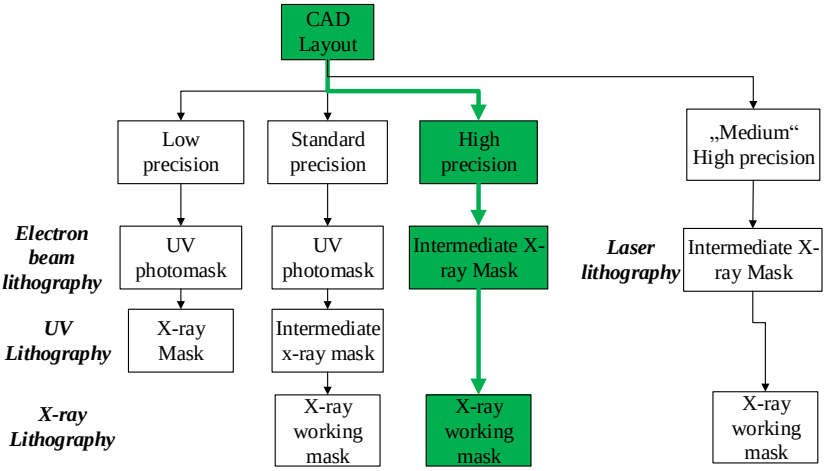

Figure 3.2: The different processes for X-ray mask fabrication. The green “route” was chosen

In this work, three optical elements were fabricated: single nickel 1D RML for 17 keV, 2D polymer compound RMLs for 34 keV, and staircase array of inclined nickel RMLs for 35 keV. For reducing the scanning time of the PSR-STHXM, the number of lenses should be as high as possible, whereas the period of RMLs which determines the spacing between neighboring X-ray foci should be minimized. Furthermore, sub μm foci size and large FoV are also the targets.

Consequently, a first optical element was designed for 17 keV with the aim to obtain sub-μm foci size, a smaller period, and a large number of lenses without focusing on the structure height. Since the fabrication process parameters for the refractive multi-lens were unknown, the fabrication limits were studied (radius of curvature). The material for the first single RML was a nickel, as its refractive index decrement is one order of magnitude larger than the epoxy-based negative photoresist.

After successfully realizing 1D RML for 17 keV, the aims were to increase the structure height and photon energies. Therefore, a 2D optical element for 34 keV was designed. In this case, the material chosen was the polymer SU-8 with 2 mm height (highest possible height for lenses, which can be realized by deep X-ray lithography). 2D RMLs should be stacked along the optical axis to minimize the focal distance due to the low refraction power of SU-8.

Finally, to perform a large FoV, a staircase array of inclined RMLs, that overcome the height limit of X-Ray LIGA fabrication was developed to achieve cm long X-ray foci. The staircase array consists of many identical single RMLs. Thus, it was made of nickel for 35 keV.

In the following, a detailed description of the fabrication process of the three X-ray optical elements used in the work is described, including the fabrication of the absorber mask made by E-beam lithography.

3.3 Fabrication of the 1D RMLs array

The goal was to manufacture 1D nickel RMLs with the smallest period (physical aperture respectively) and sub-µm radius of the parabolas' curvature. Height should be as high as possible- µm.

The requirements are:

1. The identical geometrical shape of the single lenses
2. Absence of sidewall inclination
3. Minimum web distance (distance between parabola apexes)
4. Excellent lens quality
5. The sub-µm radius of curvature (focal distance in the mm range)
6. Biconcave parabolic profiles.

3.3.1 Design

The single nickel RML was specially designed for the usage at the IMAGE beamline at the KARA synchrotron facility (KIT, Karlsruhe, Germany), taking into account its' constraints:

- The maximum photon energy is 17 keV (wavelength 0.73 Å), which limits the lens material choice to minimize the absorption [58];
- The source size (rms) is 0.93 mm × 0.0253 mm (horizontal × vertical),
- The beam size at the specimen position (8 mm horizontal × 1 mm vertical) limits the length of RML (number of single biconcave lenses in one row).

The design of the RMLs was performed using the LayoutEditor software (juspertor GmbH [https://layouteditor.com/]) and saved in the GDS II file format since this file format is supported by the electron beam writer EBPG5200Z (Raith GmbH).

Conventionally, the refractive lenses are used as compound refractive lenses, which significantly simplifies the fabrication of such CRLs. In this case, the

radius of curvature at the parabola apex is in the range of several tenths of micrometers and the physical apertures of more than 50 µm. Moreover, the web distance is in the range of 20-30 µm if low absorbing materials are used, as mentioned in the previous chapter. However, the scanning time in the PSR-STHXM can be reduced if the physical aperture (period of RML) is small enough and generates the X-ray foci in the (sub-) micrometer range.

Consequently, biconcave and plano-concave shape lenses with a period of 10 µm and a physical aperture of 9 and 5 µm were designed. The web distance between the parabola apexes was 3 µm and 6 µm. The parabolic profile (used for focusing the incoming X-rays) of the RML was designed to achieve a 0.86 µm radius of curvature for the nickel RML. A macro file for LayoutEditor software was written to create the structure geometry with identified parameters. The parabolic shape was approximated with a step of 1 nm.

No design rules exist to correct the design by considering the geometry modification induced by the different fabrication steps. Real dedicated experiments remain the best way to view the process feasibility and to obtain the designed final structures. Therefore, a test mask has been fabricated; the design parameters are summarized in Table 3-2.

The mask area was divided into 165 equal areas of 2.5 x 2 mm^2 in (total area of 50 x 50 mm^2) to include 11 different designs (rows) and 15 different dose variations (columns) on one substrate.

Table 3-2: Design parameters of the nickel RMLs to be used at 17 keV.

Shape	Parabolic profile (μm)	Period/Aperture (μm) /(μm)	Web distance(μm)	Radius of curvature (μm)
Biconcave	11.82	10 / 9	3	1.7
	11.82	10 / 9	6	1.7
	23.64	10 / 9	3	0.86
	23.64	10 / 9	6	0.86
	11.82	10 / 5	3	0.53
	11.82	10 / 5	6	0.53
	23.64	10 / 5	3	0.3
	23.64	10 / 5	6	0.3
Plano-concave	11.82	10 / 9	3	1.7
	11.82	10 / 9	6	1.7
	23.64	10 / 9	6	0.86

A dose correction was performed with Proximity effect correction (PEC), Fine layer (Sleeve) /Coarse layer (bulk) (FL/CL), and BIAS FL/CL [91]. The proximity effect is a function of backscattered electrons in E-Beam lithography, which can provide additional exposure to nearby features depending on how close or proximate one element is to another. The proximity effect depends primarily on the accelerating voltage, the substrate, the resist and process, and, most importantly, the features' size and location. PEC correction was also included in FL/CL and in BIAS FL/CL. This philosophy allows reducing the writing time as much as possible. To achieve the parabola's exact designed shape, BIAS FL/CL calculations for the 50 nm area of the parabola edge in addition to FL/CL were used.

By this detailed proximity correction scheme, it is possible to fabricate the requested structures with sufficient precision. According to design values, fifteen different dose values for E-beam writer were selected to investigate the optimum dose parameters for manufacturing the test structures. The parameter set is listed in Table 3-3.

Table 3-3: Dose optimization for e-beam lithography

Number	PEC ($\mu C/cm^2$)	Number	FL/CL ($\mu C/cm^2$)	Number	Bias ($\mu C/cm^2$)
1	600	6	650/650	11	650/650
2	650	7	700/650	12	700/650
3	700	8	750/650	13	750/650
4	750	9	800/650	14	800/650
5	800	10	850/650	15	850/650

3.3.2 X-ray absorber intermediate mask fabrication using E-beam lithography

For intermediate mask fabrication, the substrate consists of a 4-inch silicon wafer, which was coated with a carbon layer, a titanium oxide, chromium (7 nm), and a gold (15 nm) layer on top of it. Then PMMA resist of 3.2 µm height was spray-coated onto the substrate. After E-beam writing, the mask was soft baked at 180 °C for 5 minutes. PMMA resist was developed with 1:1 solution in volume; 1 vol. MIBK (methyl isobutyl ketone): 1 vol. IPA (Isopropyl alcohol) for 150 seconds. After development, the structures of the test mask were checked with an optical microscope; some microscope pictures of them are presented in Figure 3.3.

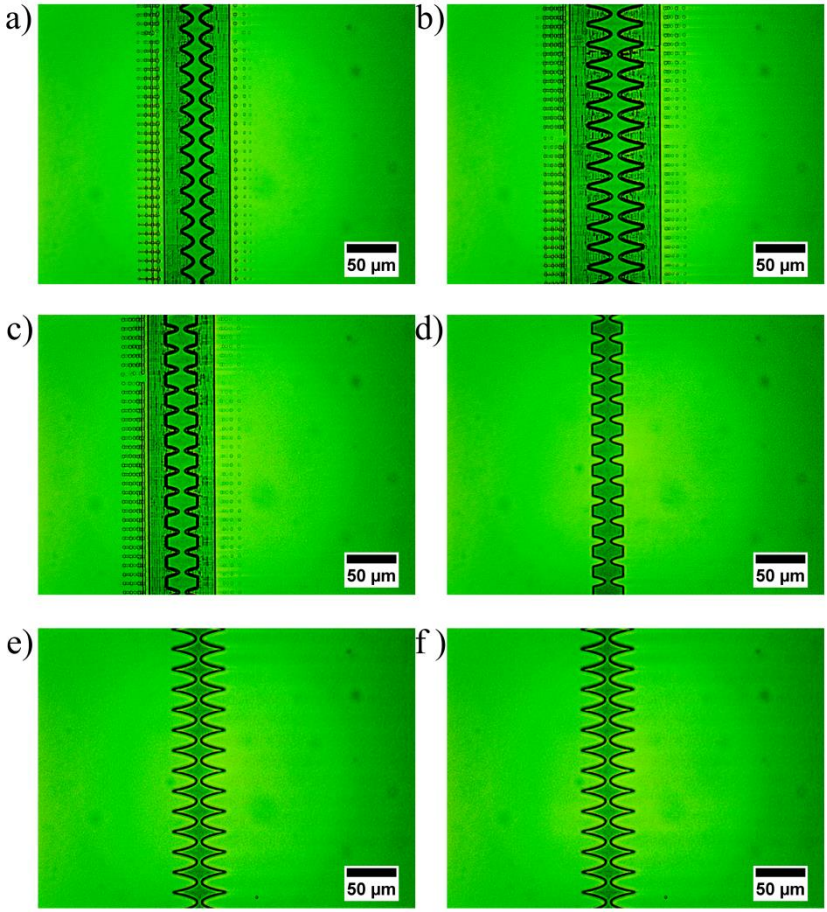

Figure 3.3: Dark green color indicates the PMMA structures, and the surrounding area would be electroplated.

After development, the intermediate mask was electroplated in a gold bath to achieve gold structure heights of about 2.2 µm. As a final step, the PMMA resist was removed.

Measurement of the gold structures using SEM was performed. They indicate that the structural dimensions that fit the designed value were achieved with a dose parameter set of:

- BIAS - FL 650 µC/cm^2 – CL 650 µC/cm^2;

As an example, SEM (ZEISS Supra 60Vp) pictures with measurements of designed structures with a period of 10 microns (physical aperture of 9 and 5 µm, web distance of 6 and 3 µm) for biconcave shaped lenses are presented in Figure 3.4.

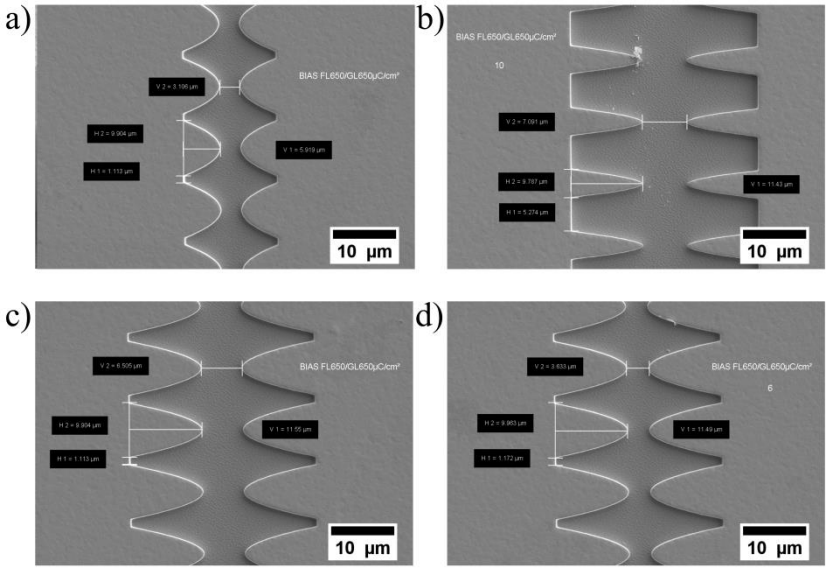

Figure 3.4: Absorber structure SEM picture of designed structures with a period of 10 microns:
(a) Biconcave, 9 µm aperture, 3.1 µm web distance.
(b) Biconcave, 5 µm aperture, 7 µm web distance.
(c) Biconcave, 9 µm aperture, 6.5 µm web distance.
(d) Biconcave, 9 µm aperture, 3.6 µm web distance.

After SEM analysis, the titanium membrane was glued on a metallic holder (4-inch) using two compound glue and was lifted off from the silicon substrate.

3.3.3 Structure fabrication

For the fabrication of nickel RMLs, a standard 525 µm silicon substrate with a titanium oxide layer with 76 µm spin-coated PMMA resist height was exposed using the intermediate mask previously described at LITHO I beamline. After exposure, the sample was developed in an organic developer GG, rinsed in BDG and DI-water, then dried in a convection oven and electroplated in a nickel bath to achieve nickel structures height of 60 µm. Finally, the PMMA resist was removed from the substrate by plasma etching (R3T GmbH). The fabrication process flow is shown in Figure 3.5

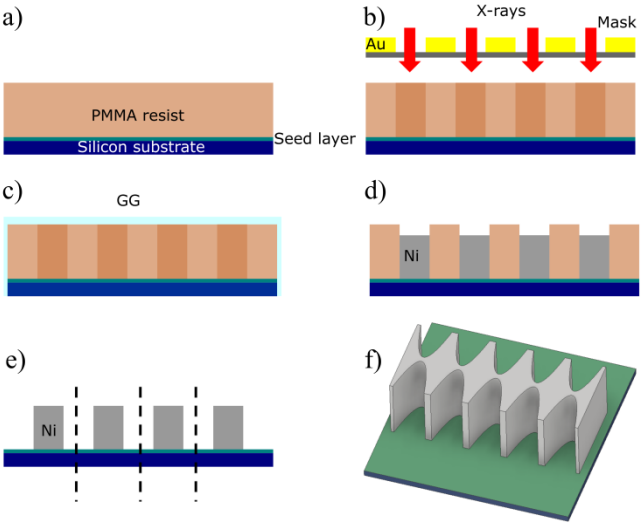

Figure 3.5: Fabrication steps to obtain the nickel 1D RML.

Nickel structures with a 10 µm period, a physical aperture of 9 and 5 µm, height 60 µm and 2.5 mm in length were achieved (see Figure 3.6). Obtained

structures were analyzed by SEM (ZEISS Supra 60Vp); the parabolic shaped lenses deviate only slightly from the design (shown later in Figure 3.6 detailed analysis), the individual focusing elements present an identical parabolic profile from top to bottom. After the SEM analysis, the substrate was cut into strips using a diamond wafer saw (Model DAD 3430, Disco Corporation, Japan) and glued on silicon pieces for further characterization and X-ray imaging.

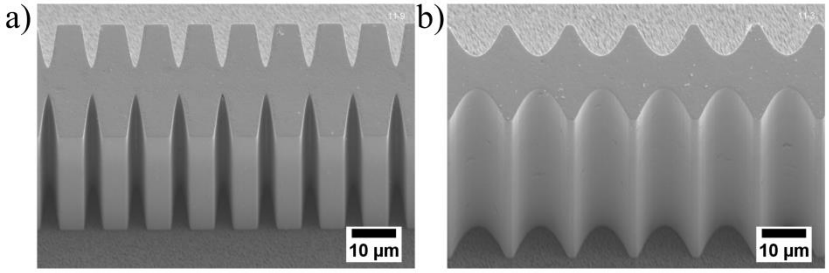

Figure 3.6: SEM picture of two different 10 µm period biconcave parabolic RMLs fabricated by DXL and electroplating
(a) Physical aperture 5 µm, parabolic profile: 23.64 µm.
(b) Physical aperture 9 µm, parabolic profile: 11.82 µm.

Since all fabricated nickel structures have been manufactured with good quality, it was necessary to select one for X-ray imaging experiments at the IMAGE beamline KARA synchrotron facility. Thus, among the fabricated structures with various parameters (physical aperture, web distance, radius of curvature) given in Table 3-1, one of the RML has been chosen that should theoretically generate the smallest diffraction-limited X-ray line foci (d_{diff}) at 17 keV. Since the RML with about 5 µm web distance was damaged after cutting, the 10 µm period biconcave RML with 9 µm physical aperture, 8.5 µm web distance, and 0.83 µm radius present the best parameters to obtain the smallest line foci.

A detailed characterization of the geometrical size of this RML (see Figure 3.7) was done by using SEM (Zeiss Supra 60 VP). The fabricated nickel structures are free of shape deviations, sidewall inclination, cracks, and de-

fects. The single lenses present identical parameters within the complete length (2.5 mm).

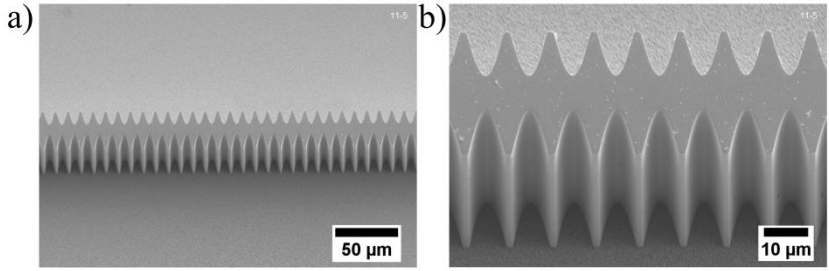

Figure 3.7: SEM images of the selected 1D RML (overview and detailed view) [36]

In Figure 3.8, the comparison of the designed RML (black dots) from the fabricated structures (red dots with error bars) is presented. The form of the fabricated RML is in excellent agreement with the design. The small deviations are caused by PMMA resist swelling during the electroplating process. The web distance between parabola apexes enlarged from 6 µm to 8.5 ± 0.17 µm, and the physical aperture is 8.95 ± 0.23 µm. The radius of curvature was estimated to be 0.83 µm (design value was 0.86 µm).

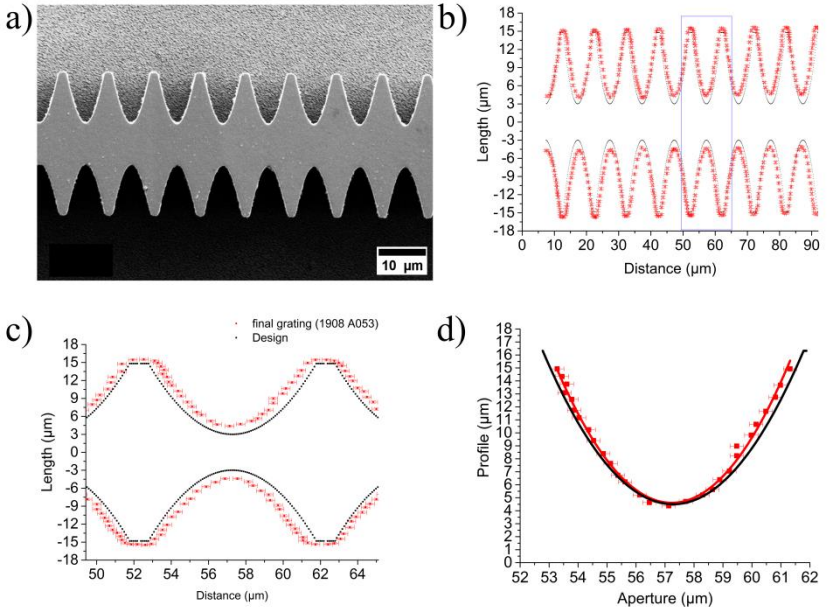

Figure 3.8: Analysis of the deviation of the fabricated structures from the design values [36]:
(a) SEM image of RML fabricated by deep X-ray lithography and electroplating (top view).
(b) Comparison of the fabricated structures (red) with the design values (black). The period of the RML is the same as the design value (10 µm).
(c) Zoom-in view of the blue rectangle in (b). The web distance between parabola apexes increased from 6 µm (design value) to 8.5 µm
(d) Designed parabolic profile (black curve) in comparison to the fabricated parabolic shape with parabolic curve fitting (red). The fabricated structures' profile is narrower than the designed one, and the radius of curvature changed from 0.86 µm (design value) to 0.83 µm.

To summarize, the parameters of the chosen lens are:

- Period: 10 µm,
- Physical aperture: 8.95 ± 0.23 µm,
- Radius of curvature: 0.83 ± 0.2 µm,

- The number of single lenses: 250 (2.5 mm length)
- The web distance between parabola apexes: 8.5 ± 0.17 µm
- Height: ca. 60 µm.

According to this analysis, the slight deviation of the fabricated RML may lead to the enlargement of the theoretical diffraction-limited X-ray line foci size (FWHM). Another parameter that contributes to the enlargement of the X-ray line foci size is the sidewall surface roughness [59]. The surface roughness required for the refractive lens should be below 100 nm [73]. The roughness of the sidewall of the fabricated nickel RML was measured with an optical three-dimensional surface profiler (ContourGT, Brucker, USA) using the vertical scanning interferometry mode with a luminous green source. An area of 80 µm x 150 µm was measured, and the average surface roughness (Ra) was evaluated to be 36 nm ± 5 nm (see Figure 3.9)

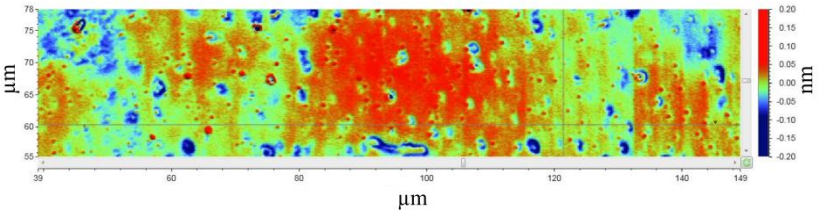

Figure 3.9: The measured surface roughness of the fabricated 1D RML.

3.4 2D compound lens array made of SU-8 for 34 keV by DXL

Due to the fact that the fabrication of single 1D RMLs with the sub-µm radius of curvature and height up to 200 µm remains a highly challenging task, one solution consists in using many lens elements with a larger radius of curvature stacked along the optical axis. This lens is called a compound refractive lens (CRL). Since DXL allows to fabricate only 1D CRLs, to obtain a 2D point focus CRLs, two 1D CRLs have to be mounted, one of them ro-

tated by 90^0 around the optical axis and connected in an interdigitated way [83][84].

2D CRLs are widely used for synchrotron applications. They consist of a large number of individual lens elements to achieve short focal lengths. CRLs are frequently used in the photon energy range between 8 keV and 100 keV.

3.4.1 Design

The 2D CRMLs (compound RMLs) were specially designed for an X-ray energy of 34 keV and the PSR-STHXM using the Medipix Merlin 3.0 photon-counting detector (FoV 14 mm x 14 mm, 256 × 256 pixels, 55 µm pixel size, CERN, Geneva, Switzerland) working in charge summing mode [85]. Consequently, the focal points grid period has to be equal to the pixel pitch of the detector, so the individual CRMLs physical apertures are 55 µm × 55 µm. A 2D CRMLs of 34 × 34 single CRLs, resulting in a total entrance aperture of 1.87 mm × 1.87 mm, is designed and should be fabricated in 2 mm high photoresist.

The design parameters of 2D CRMLs are described and given in Figure 3.10. Each lens element has two rectangular stabilization parts with b = 40 µm at the edges of each RML, resulting in a total lens element width of 34 · 55 µm + 2 · 40 µm = 1950 µm.

The web distance w = 25 µm was chosen to obtain mechanically stable lens elements. With air gaps d = 50 µm between neighbor lens elements along the optical axis, this results in 2D CRMLs with a total length of L_{CRML} = 22.5 mm calculated by:

$$\mathrm{L_{CRMLs}} = 2(\mathrm{N_v} + N_h)\frac{1}{\mathrm{R_{v,h}}}\left(\frac{\mathrm{A_{ph\,(v,h)}}}{2}\right)^2 + (\mathrm{N_v} + N_h)\mathrm{w} + ((\mathrm{N_v} + N_h) - 1)\mathrm{d} \quad (3.1)$$

The designed focal length $f_{\mathrm{v,h}}$ of this CRMLs is given by [74]:

$$f_{\mathrm{v,h}} \approx \frac{R}{2\delta(N_{\mathrm{v}}+N_h)} + \frac{L_{\mathrm{CRL}}}{6} \approx 360\ \mathrm{mm}, \quad (3.2)$$

using a refractive index decrement of $\delta \approx \frac{0.000281}{(\mathrm{E}\,/\,\mathrm{keV})^2} \approx 2.43 \times 10^{-7}$[86].

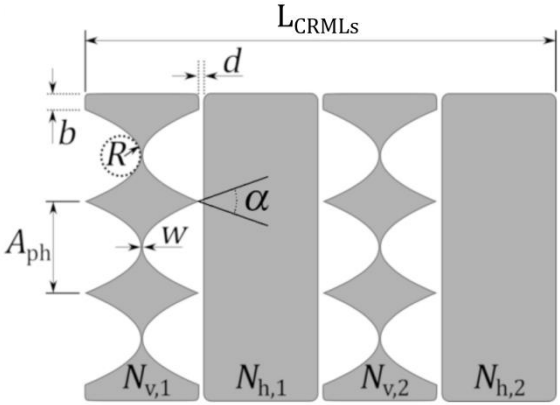

A_{ph}	55 µm
N_v	46
N_h	46
R	15.9 µm
d	50 µm
α	60^0
w	25 µm
b	40 µm
L_{CRL}	22.5 mm

Figure 3.10: The design parameters of 2D biconcave parabolic polymer (SU-8) CRMLs for 34 keV: A_{ph} – physical aperture, N_v and N_h number of lens elements in vertical and in a horizontal direction along the optical lenses, R – radius of curvature, d is an air gap, α – the angle between adjacent parabolas, w – web distance, b – rectangular parts at the edges for stabilizing the RMLs, L_{CRMLs} the total length of the CRMLs [37].

3.4.2 Fabrication

The fabrication process flow of DXL of the 2D polymer RMLs is shown in Figure 3.11. A 525 µm thick 4" Si wafer coated with 2000 µm thick resist was exposed at the LITHO II beamline at the KARA synchrotron facility, and the structures were developed. Parallel rows of 1D RMLs were obtained. To make the 2D RMLs, the rows were separated by cutting the silicon wafer with a diamond wafer saw. Then two 1D RMLs were mounted in an interdigitated way under 90^0, aligned, and connected by gluing two L-shaped invar steel blocs [82].

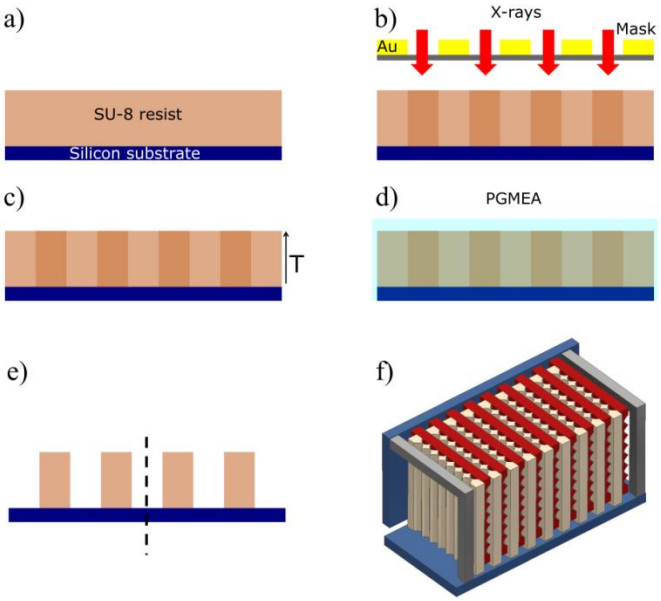

Figure 3.11: Schematic overview of the fabrication of a 2D array of CRLs by DXL using SU-8 resist. The mask consists of the gold structures on the top of the Ti-membrane.

Optical microscope images of the final component are presented in Figure 3.12. Due to the fact that resist is non-conductive, it was not possible to perform accurate structure measurement using SEM. However, optical microscope inspection and X-ray characterization (see 4.2) indicate that the structure dimensions agree well with the designed values.

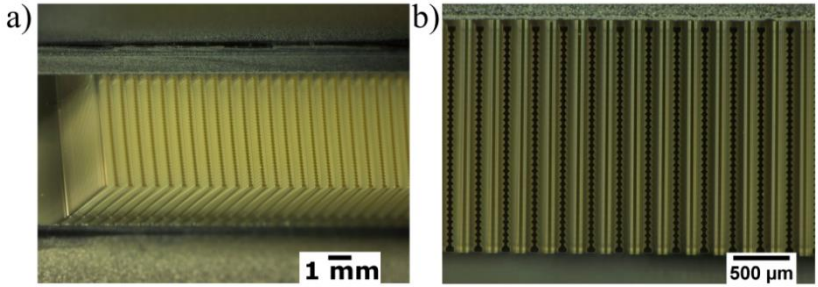

Figure 3.12: Optical microscopy image of the 2D compound RMLs. (a) side view (b) top view [37]

3.5 Inclined 1D multi-lens array

In the previous chapters, the fabrication of the 1D and 2D X-ray optics was presented. The height of the RMLs was limited by the photoresist height (max. 2.5 mm). In the following, a new type of X-ray RMLs is described, which overcomes the fabrication limits of the 1D RMLs and Compound RMLs already presented. The principle of increasing the length of X-ray line foci by an array of one-dimensional RMLs is presented in Figure 3.13. The idea is to utilize an array of inclined RMLs with regular intervals d and uniform height h. Furthermore, the inclination angle β of all RMLs is identical on the substrate. Consequently, tilting the substrate with an angle $\alpha = 90^0 - \beta$ relative to the beam, the RMLs are oriented perpendicularly to the incoming X-ray beam and are positioned over the whole FoV_h within a staircase-like arrangement. Moreover, in the transition area $t\,(t = h - d\cos\beta)$, the top part of one RML and the bottom part of the adjacent RML contribute to the focusing of the incoming X-ray beam as a single biconcave refractive lens. Therefore, under monochromatic plane wave X-ray illumination, the RMLs produce X-ray line foci with a length in the centimeter range, which is defined by the number of RMLs (Figure 3.13 (a)). Whereas in the perpendicular direction in Figure 3.13 (b) (specimen

scanning direction), the FoV_v is equivalent to the number of lenses in a single RML.

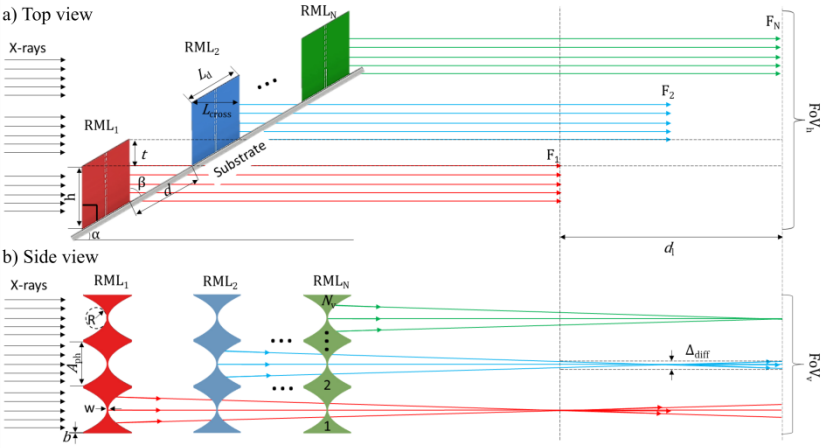

Figure 3.13: Principle and design parameters of the staircase array of inclined RMLs for large FoV PSR STHXM. (a) top view, (b) side view. d – the regular interval between RMLs, Δ_{diff} – diffraction-limited line width, FoV_h, and FoV_v – horizontal and vertical FoVs in the detector plane, respectively, F_i (i = 1, 2, …, N) – the focal positions for each RMLs starting from RML_1, w – web distance, A_{ph} – physical aperture, R – radius of curvature, b – the distance between neighboring parabolas, α – tilt angle of the substrate, β – inclination angle of the RML with respect to the substrate, L_d – design length of the single lens, Lcross – length of the lens along with X-rays, h – the height of the RMLs when the substrate is tilted, t – transition zone where two RMLs contribute to form line foci, d_f– a depth of field, N_V is the number of individual lenses in each RML [38].

3.5.1 Design of a staircase array of inclined RMLs

The staircase array of inclined RMLs (inclined RMLs hereafter) was designed for the demonstration of PSR-STHXM with a large FOV (in the centimeter order) and sub-μm spatial resolution, at BL20B2/ SPring-8 synchrotron facility (Japan) at 35 keV. Each RML consists of biconcave parabolic lenses (Figure 3.13 (b)) [59][73]. Accordingly, the design length of the lens L_d is:

$$L_{\mathrm{d}} = \frac{1}{R} \cdot \left(\frac{A_{\mathrm{ph}}}{2}\right)^2 + w, \tag{3.1}$$

where R is a radius of curvature of a parabola, A_{ph} is the physical aperture and w is the web distance w. Accordingly, when the substrate is tilted at an angle $\alpha = 90^0 - \beta$, the length of the X-ray path through an RML, $\mathrm{L_{cross}}$, is:

$$L_{cross} = L_{\mathrm{d}} \cdot \cos\alpha \tag{3.2}$$

The focal distance F of each RML is defined as:

$$F = \frac{R}{2\delta}, \tag{3.3}$$

where δ is the refractive index decrement and for the nickel at 35 keV, $\delta = 1.44 \times 10^{-6}$ [87].

The width of the diffraction-limited X-ray line foci (FWHM) is given by equation 2.20. The depth of focus (*DoF*) of the single RML has to be large enough to achieve sub-µm focal width (FWHM) within the depth of field d_l ($> F_{\mathrm{N}} - F_1$ see Figure 3.13), and is given by equation 2.19. The design parameters are listed in Table 3-4.

Table 3-4: Design parameters of inclined RMLs.

	β deg.	h µm	N_{v}	N	d µm	w µm	L_{d} µm	A_{ph} µm	R µm
Design	60°	114	2000	189	150	3.5	114.3	24	1.3

The vertical FoV_{v} in the specimen scanning direction and a horizontal $\mathrm{FoV_h}$ are given by:

$$FoV_{\mathrm{v}} = N_{\mathrm{v}} \cdot (A_{\mathrm{ph}} + b) \text{ and } FoV_{\mathrm{h}} = N \cdot h, \tag{3.4}$$

where N_V is a number of lenses in single RML, b is the distance between adjacent parabolas, and N is the number, and h is the height of inclined RMLs.

3.5.2 Determination of the influence of fabrication tolerances and substrate misalignment on the focusing performance in the transition zone

The area where the rays pass two lens elements is called a "transition zone." To investigate the influence of alignment errors and manufacturing tolerances on the optical performance of the RMLs in the transition zone *t*, ray-tracing simulations have been performed using the commercial software Zemax (Zemax, LLC, Delaware limited liability company, USA). For the simulations, the following parameters have been used:

- X-ray energy: 35 keV
- Material: Nickel
- Height of RMLs: 118 ± 2 μm
- Interval between RMLs: 150 μm
- Number of RMLs: 2
- Number of individual lenses in one RML: 3
- Physical aperture: 24 μm
- Inclinational angle of the RMLs β: 60^0
- Substrate tilting angle α: $30^0 \pm 0.2^0$

Figure 3.14 presents the simulation results. Incoming rays passing two RMLs with the ideal parameters (uniform height, the perfect interval between RMLs) are focused just as well as rays which pass through only one individual lens element. The perfect RMLs generate three parallel focused line foci, shown by the red lines in Figure 3.14 (a). The distance between two neighbour line foci is 24 μm, which equals the aperture of the lenses. The yellowish region indicates the intensity level of the incoming rays. The background level around the line foci in the transition area is in the range of 10^{-6} of the focused intensity.

However, the manufacturing of the inclined nickel RMLs results in an inhomogeneous structure height. Therefore, to simulate the effects of such a height deviation, a height difference of 2 µm between adjacent RMLs was studied. The length of a transition zone is 61 µm when the substrate with 118 µm high RMLs perpendicular to the substrate (which gives 136 µm when the structures are perpendicular to the beam) is tilted by 30^0. As shown in Figure 3.14 (b), in this case, a background pattern reaching the tenfold intensity of the incident beam intensity is produced.

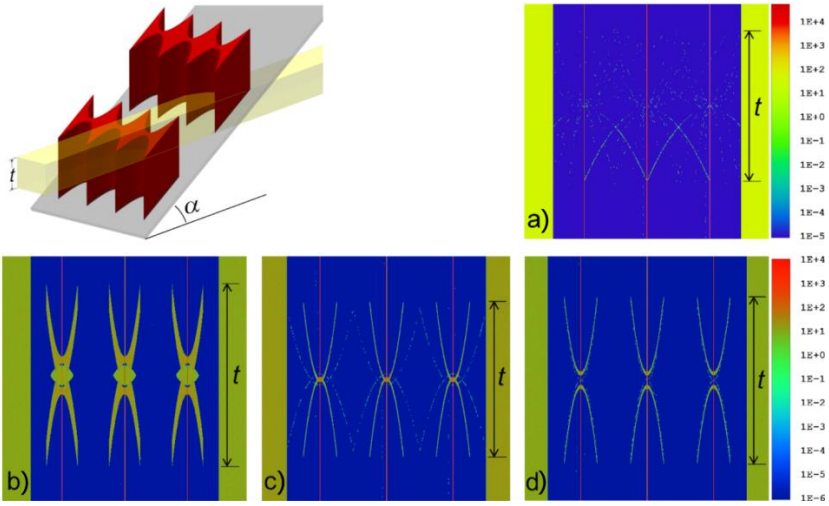

Figure 3.14: Ray-tracing simulation of the intensity distribution in the transition area t of the ideal inclined RMLs made of nickel at an X-ray energy of 35 keV (a). The background pattern is prominent when neighbour RMLs have a 2 µm height difference (b). Background pattern when the substrate is not perfectly inclined by $\alpha = 30°$, but by $\alpha = 29.8°$ (c) respectively $\alpha = 30.2°$ (d) [38].

Another parameter to be considered is a substrate tilting angle α. Thus, the influence of the substrate misalignment was also simulated and is shown in Figure 3.14 (c) and (d) when $\alpha = 29.8°$ and $30.2°$, respectively. The misalignment of the substrate also produces a background pattern with a maximum intensity in the range of the tenfold intensity of the incident beam intensity. However, the substrate tilting angle could be as precise as 0.02^0 using a

state of the art positioning system (goniometers). The simulation show, that the fabrication tolerances and substrate misalignment assumed lead to a maximum background intensity in the range of 10^{-3} of the focus line intensity. So if the height of RMLs is uniform and constant, for instance, by a polishing procedure after the electroplating and by inclining the substrate to the angle of 30° with a deviation tolerance of better than 0.2° the unwanted intensity background generated will be at an acceptably low level.

3.5.3 Fabrication

The intermediate mask is processed using the standard procedure, but the working mask with a higher absorber structure must be processed using the same way as the final structuring: tilted aligned exposure, as presented in Figure 3.15. Alignment is necessary to obtain the designed structure. The structure on the working mask must be inclined (with the same angle as the one used for structuring) to avoid X-ray exposure shadowing which will destroy the structure shape. The tilted exposure DXL is performed by tilting the substrate and the working mask for an angle α accordingly. Next, the resist pattern with the structures inclined at an angle $\beta=90^0 - \alpha$ is developed in a GG solution, rinsed in BDG and DI water, and dried. Then, the nickel RMLs are created by an electroplating process. Since the height of RMLs should be uniform, as shown in the previous section, the sample should be grounded and polished. The polishing process is performed by keeping the resist on the substrate to prevent structures from falling and damaging due to the polishing machine's applied mechanical forces. After obtaining the desired RMLs height, the PMMA resist is removed by a flood exposure and repeating the development process.

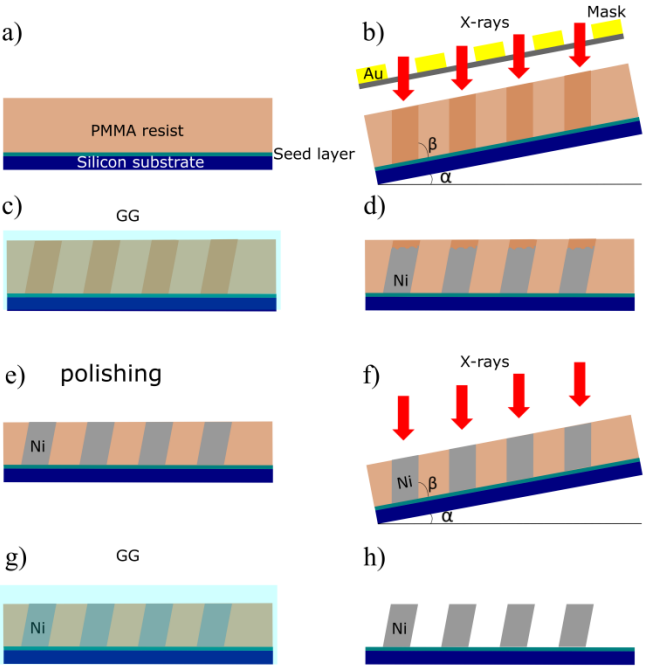

Figure 3.15: Fabrication of the inclined RMLs via tilted exposure DXL and electroplating

3.5.4 Design and fabrication of the X-ray mask

The design of the intermediate mask was done, taking into account the PMMA resist swelling. Also, the proximity effect correction of 378000 biconcave lenses by the e-beam writer is possible but will take too long processing time (several weeks). Therefore, to obtain the physical aperture of 24 µm, the parabolic profiles were corrected by subtracting 1 µm, as shown in Figure 3.16 a). After correction, the aperture's designed value is 23 µm, and the distance between two parabola apexes is 3.5 µm respectively. The period of the RML was 25 µm. The number of biconcave lenses in one RML is 2000, which represents 5 cm in length. The distance between RMLs is 150 µm. The number of RMLs is 189. The designed length of a single lens is

114 µm. Therefore, the design area of the mask covers 5×5 cm^2 (Figure 3.16b). Four alignment markers were also included in the design. Their function is to align the gold absorber mask in the scanner for the tilted exposure DXL. The photo of the fabricated mask is shown in Figure 3.16c.

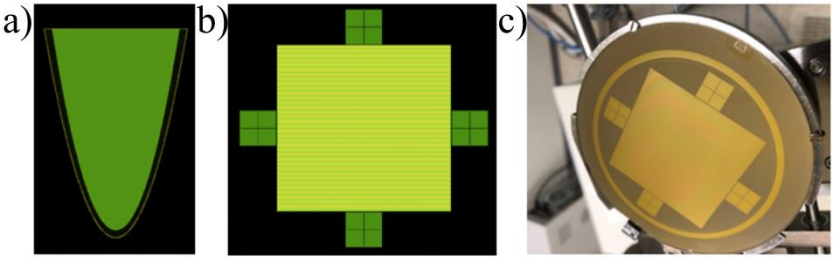

Figure 3.16: Correction of the parabolic profiles for 1 µm. Yellow – desired parabolic shape, green – corrected one. b) full design of the intermediate mask for the inclined RMLs. c) Fabricated intermediate mask.

3.5.5 Tilted Exposure DXL

The tilted exposure DXL was performed using the working mask with the 25 µm gold absorber structures at the LIGA II beamline/ KARA synchrotron. Samples with an average height of 220 µm were exposed. Different exposure parameters and development time were tested; the ones for which the structure quality after development were successful are summarized in Table 3-5.

Table 3-5: Exposure parameters and development time

Sample	Filter	Exposure dose mA min/cm^3	Development time (h)
LFOV_2	125 µm+25 µm Kapton + 15 µm Ni	9000	8
LFOV_3	125 µm+25 µm Kapton + 15 µm Ni	8000	12
LFOV_4	125 µm+25 µm Kapton + 15 µm Ni	10000	10

After development and drying, the samples were electroplated in a nickel bath at 55°C. It should be mentioned here that the quality control of the fabricated structures (structure shape, height) can be done only after removing the

resist. Some samples were electroplated using the calculated time to obtain the desired thickness; the risk is that the specified height will not be reached. To obtain the desired height, the structure is overplated; then, the top surface (electroplating front) is typically lapped and polished to the needed thickness, here 118 ± 4.2 µm. The risk is that the structure will be damaged. The comparison of the fabricated polished sample "LFOV_2" and unpolished sample "LFOV_4" is illustrated in Figure 3.17.

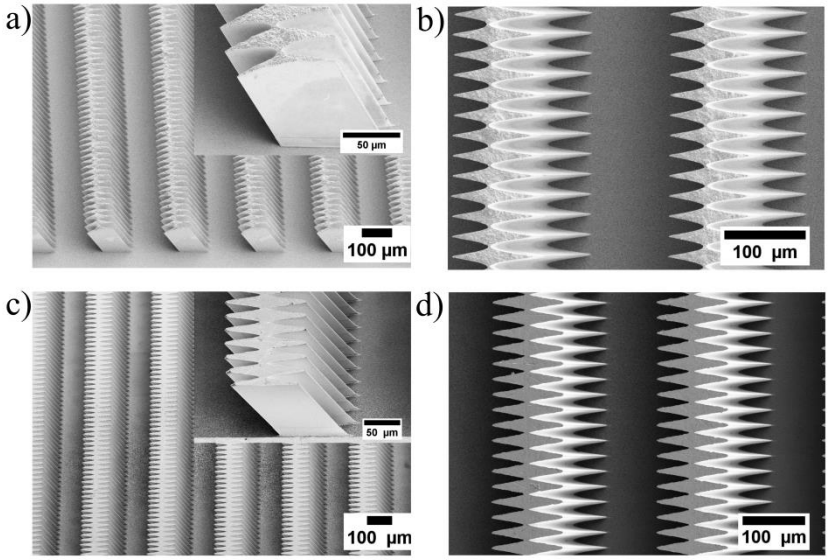

Figure 3.17: (a) (b) SEM images of the unpolished sample "LFOV_4". (c) (d) SEM images of the polished sample "LFOV_2" [38]

The fabricated parameters of the inclined RMLs presented in Figure 3.17 are listed in Table 3-6; the designed ones are again presented for comparison.

Table 3-6. The parameters of the fabricated inclined RMLs

	β, Deg.	h, µm	N_v,	N,	d, µm	w, µm	$L_{d,}$ µm	A_{ph} µm	R, µm
Design	60°	114	2000	189	150	3.5	114.3	24	1.3
Unpolished sample LFOV_4	59.8 ±0.2°	123±15	2000	189	150 ± 0.2	4.56	110	24	1.4
Polished sample LFOV_2	59.8 ±0.2°	118 ± 4.2	2000	189	150 ± 0.2	4.56	110	24	1.4

The structure quality and geometry present an excellent agreement with the designed structure. As a result, 378000 identical nickel lenses with almost uniform height with an inclination angle of about 60^0 were achieved. -

Therefore, it is possible to realize a large FoV PSR-STHXM (see section 5.3)

4 X-ray characterization at synchrotron facilities

The focusing performance of the fabricated refractive multi-lenses (RMLs) described in the following chapter is evaluated by using monochromatic hard X-ray beams (≥ 17 keV) through the acceptance of beam time proposals at different synchrotron sources; the RMLs have been specially designed for each beamline and tested at the corresponding facility.

The RMLs are characterized by their focal distance, periodicity (distance between neighboring lines), size of the diffraction-limited line (point) foci at the focal distance, spectral intensity enhancement (intensity gain). The knowledge of these parameters is necessary to perform further imaging experiments. For example, the specimen scanning in the PSR-STHXM is defined by the measured/evaluated spot size and not the theoretical ones.

Either direct imaging or knife-edge measurement scans were performed for the characterization of the RMLs.

Direct X-ray imaging is done using high-resolution indirect detectors consisting of scintillator crystal, magnification optics, and CCD or sCMOS camera [6]. The focused X-ray beams impinge the scintillator crystal and is converted into visible light, which is then registered by the high-resolution camera with an effective pixel size in the range of about 0.6-0.9 μm. Direct imaging is useful for the alignment of X-ray optics. In addition, by moving the indirect detector along the optical axis, the focal distance is determined. The size of the line (point) foci measured by the CCD-camera is a convolution of the real foci size with the resolution of the scintillator crystal and the detector's effective pixel size. Hence, high-resolution scintillator crystals – Cerium activated Lutetium Aluminium Garnet (Lu3Al5O12:Ce) and Tb-doped Lu2SiO5 (LSO:Tb) - were used [7]. The direct imaging technique, which is

presented in Figure 4.1, was used to study the focusing performance of the 1D RML and 2D compound RMLs.

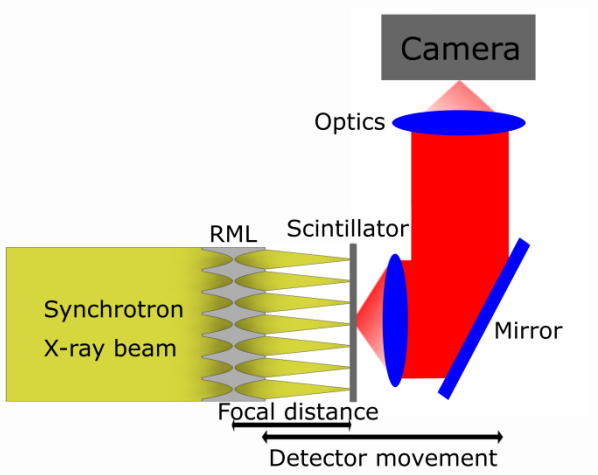

Figure 4.1: Direct imaging of the X-ray line and point foci using the high-resolution indirect detector.

The knife-edge technique, which is presented in Figure 4.2, was used to evaluate the size of the X-ray beams generated by the staircase-array of inclined RMLs. The knife-edge technique is based on a strongly absorbing sharp-edge (slightly tapered Tantalum blade) which is moved through the X-ray line foci perpendicular to the optical axis; the X-ray intensity is recorded by the camera. The focal distance was defined by performing a knife-edge scan at different positions along the beam axis, searching for the minimum of the focal width (FWHM). The focal width (FWHM) is calculated using the derivative of the knife-edge scan intensity profile and subsequent Gaussian fitting, which delivers the width of the X-ray line foci (see Figure 4.2).

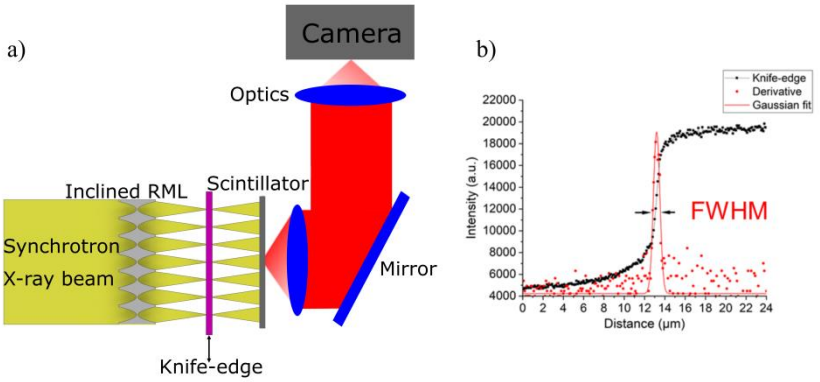

Figure 4.2: Schematics of the knife-edge scan (a) and evaluation of the size of the X-ray beam (b). An intensity profile as a function of the knife-edge position (black dots) and its derivative (red dots) are presented. The line foci width is given by the FWHM of the Gaussian fit. For the simplification of the sketch, only one inclined RML is shown.

In the next sections, the evaluation of the focused X-ray beams generated by developed X-ray optics is described.

4.1 Characterization of 1D RML at IMAGE beamline/KARA (Germany) synchrotron facility at 17 keV

1D RML were characterized by direct imaging at the wiggler IMAGE beamline at the KARA synchrotron radiation facility (KIT, Karlsruhe, Germany) (see Figure 4.3). 17 keV monochromatic X-rays were generated by a Si (111) double crystal monochromator, placed 15.5 m from the source. To evaluate X-ray line foci, a 74 μm LSO:Tb scintillator combined with 10 x magnification optics and a PCO.edge5.5 sCMOS camera (PCO AG, Kelheim, Germany) with an effective pixel size of 0.65 μm was used. The FoV of the detector was 1.66 (vertical) × 1.4 mm^2 (horizontal). The exposure time was 10 s. The

RML was oriented vertically, as shown in Figure 4.3, since the source size in the vertical direction is much smaller than the one in the horizontal direction.

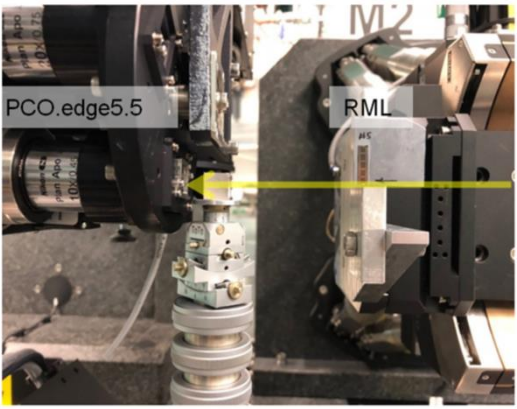

Figure 4.3: Photo of the experimental setup.

Figure 4.4 shows the results of the characterization. The length of the X-ray line foci is 60 µm, equal to the height of fabricated RML. All intensity profiles are almost identical. The measured focal distance was 67 mm, which is in good agreement with the theoretical value (69 mm).

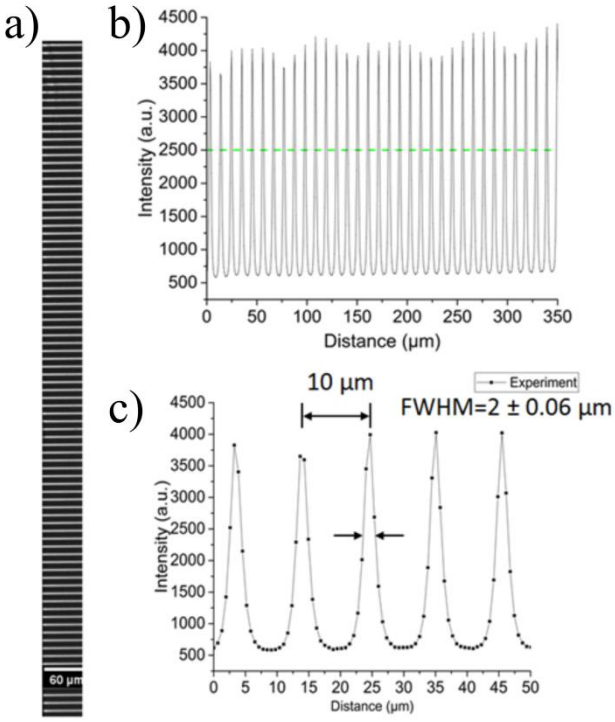

Figure 4.4: X-ray characterization results: (a) X-ray focused lines generated by the RML measured at 17 keV. (b) Profiles of line foci and (c) close-up view. The Green dashed line indicates the incoming beam intensity. The distance between foci is 10 µm, and the s spacing, which is beneficial for the PSR-STHXM proof of concept demonstration (Chapter 5) [36].

The spectral intensity enhancement (SIE) is defined as the ratio of radiation powers through a chosen reference area at the location of the smallest beam dimensions with and without the X-ray optical system [88][89]. Using an area of 60 µm × 2 µm, the measured SIE is 1.5, which is a factor of 3 smaller than the ideal one (9 µm physical aperture/2 = 4.5) due to the low transmission (about 33 %) of the nickel RML at 17 keV. However, the X-ray line foci width (FWHM) is about 2 µm. All intensity profiles are identical with a period of 10 µm corresponding to the period of 1D RML.

4.2 Characterization of the 2D compound RML at B16/Diamond light source (England) at 34 keV

The characterization of the 2D compound RMLs (2D CRMLs hereafter) was performed at the B16 bending magnet test beamline of the Diamond Light Source (Harwell, United Kingdom). A channel-cut monochromator, based on a Si (311) crystal, placed 20 m from the source, was used to generate 34 keV monochromatic X-rays with an energy resolution of $\Delta E/E = 10^{-4}$. Point foci were measured by direct imaging using a high-resolution indirect detector consisting of a 5 μm thick LuAG: Eu scintillator (FEE, Idar-Oberstein, Germany) combined with 10x magnification Olympus UPlanSApo microscope objective, an Optique Peter microscope system, and a pco.4000 CCD camera with 4008 × 2672 pixels (PCO AG, Kelheim, Germany). The effective pixel size was of 0.9 × 0.9 μm^2 and, thus, the FoV of the detector was 3.6 (vertical) × 2.4 mm^2 (horizontal). The 2D CRMLs were placed on a motorized hexapod allowing for precise alignment in x-, y-, z-directions. Figure 4.5 (a) shows the shadow projection image of the generated X-ray point foci at the focal plane with a period (distance between neighbouring foci) of 55 μm corresponding to the physical aperture of 2D CRMLs. The focal distance was determined by moving the detector along the optical axis. Each intensity spot was analyzed by 2D Gaussian fitting for various detector positions along the optical axis to evaluate the smallest size of the X-ray intensity. Thus, the focal distance was determined to be $f_{\mathrm{exp,v,h}} = (362 \pm 3)$ mm. This is in an excellent agreement with the theoretical value of $f_{\mathrm{v,h}} \approx 360$ mm.

The evaluated average focal point foci size (FWHM) is 3.55 ± 0.62 μm (horizontal) and 2.10 ± 0.81 μm (vertical). The measured results are presented in Figure 4.5 (b) (c) as contour plots. The point foci size (FWHMs) differs in the horizontal and vertical direction due to the synchrotron source shape. The point foci' horizontal size is smaller in the central region and increases towards the boundaries of the 2D CRMLs substrate.

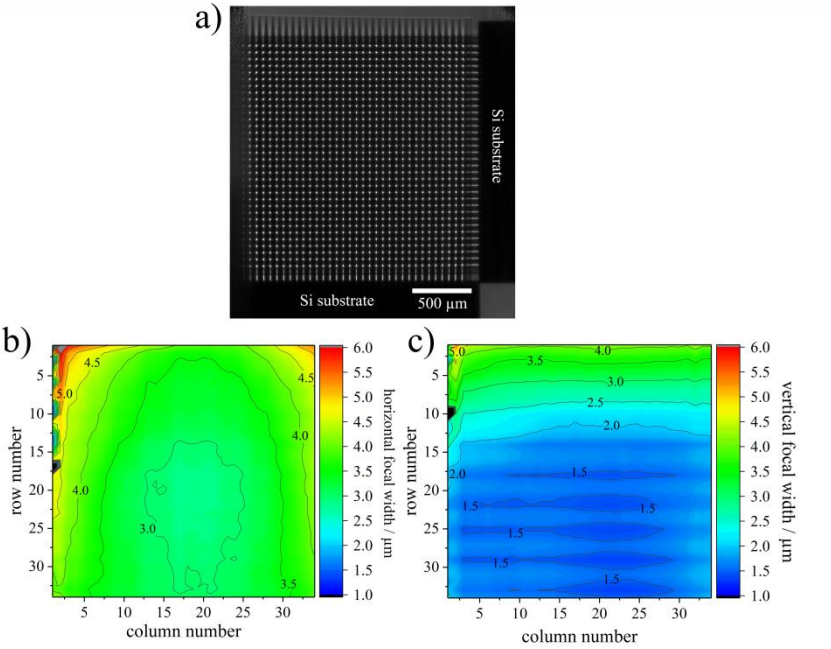

Figure 4.5: (a) High-resolution detector image of the 34 × 34 point foci of the 2D CRMLs with the silicon substrates to the right and bottom. Measured X-ray point foci size (FWHM) in horizontal (b) and vertical (c) directions. The ordinate states the row number of subCRLs, abscissa states the column number of subCRLs [37].

The average SIE is 16, which was determined by using a reference area of 1.8 µm × 1.8 µm for the 34 keV X-ray beam. As presented in Figure 4.6, the SIE in the central region of 2D CRMLs is higher, matching the X-ray point foci sizes (see Figure 4.5 (b)). At the first and second subCRL column, the SIE is weak due to the shadowing caused by a small misalignment of one mounting frame connecting the two 1D half lenses. An average 2D CRMLs transmission $T_{\mathrm{avg}} = 65.8\,\%$ was measured by using the SIE for a 55 µm × 55 µm reference area.

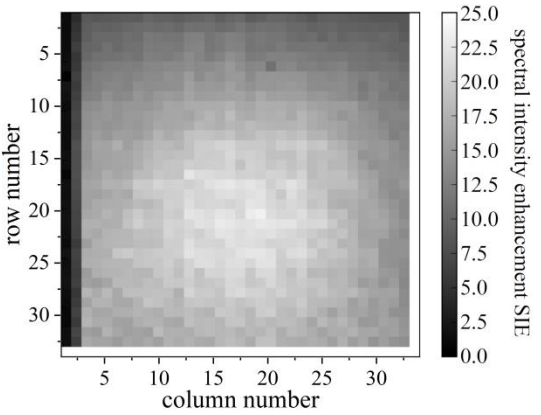

Figure 4.6: Spectral intensity enhancement (SIE) of the 34 × 34 periodic point foci array at the focal plane, using an area of 1.8 μm × 1.8 μm for the evaluation (E = 34 keV) [37].

4.3 Characterization of the inclined RMLs at BL20B2/ SPring-8 synchrotron facility (Japan) at 35 keV

The characterization of the staircase array of inclined RMLs was done at the medium-length bending magnet beamline BL20B2 since it provides a beam size of about 300 mm (horizontal) × 20 mm (vertical) at the sample position. The beam flux density of 35 keV monochromatic X-rays is ~10^8 photons/s/mm^2. The substrate with inclined RMLs was oriented vertically and tilted for 30^0 around the z-axis. Thus all of the inclined RMLs were positioned perpendicularly to the incoming X-ray beam. The focal distance was evaluated by moving a knife-edge 455 mm to 580 mm from the RMLs along the optical axis and performing a knife-edge scan at each position, searching the minimum of the focal width (FWHM). To measure intensity response through the knife-edge scan, an sCMOS camera (Hamamatsu Photonics ORCA-Flash 4.0) coupled with a set of optics and a 200 μm-thick LuAG scintillator was used. The number of pixels of the camera was 2048 × 2048, and the effective pixel size was 8.03 μm. A slightly tapered

Tantalum blade was used as the knife-edge and was scanned through the foci with a step size of 100 nm. The experimental setup picture is presented in Figure 4.7.

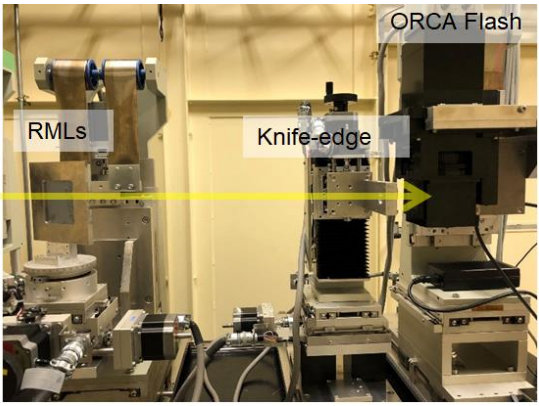

Figure 4.7: Experimental setup picture. The staircase array of inclined RMLs oriented vertically.

The camera was placed at 50 mm behind the knife-edge. Figure 4.8 (a) shows one of the images recorded by the sCMOS camera. For an orientation of the RMLs perpendicular to the beam, the effective height h_{eff} ($h_{\text{eff}} = h\text{-}t$) was measured to be 112 µm (14 pixels with 8 µm size), and the transition zone is 24 µm (3 pixels), respectively. Since the fabricated inclined RMLs had a slight variation of the structures' height, even after polishing, the periodic pattern can be observed. However, the analysis of the intensity profiles in the regions h_{eff} and t revealed that the idea for increasing the height of the focused X-ray beam by two neighboring RMLs is valid (Figure 4.8(b)). The intensity peaks coincide, and the distance between them is 24 µm. However, the intensity in the transition region t is slightly lower, as predicted by the ray-tracing simulations (see 3.5.2).

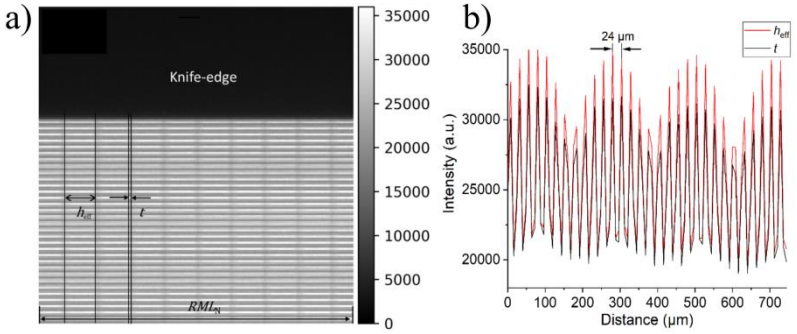

Figure 4.8: (a) One of the recorded images in the knife-edge scan; (b) Intensity profiles through the RMLs within h_{eff} and transition area t in (a). The distance between intensity peaks is 24 μm [38].

The measured values of the focal width (FWHM) obtained by the knife-edge measurements at different distances are shown in Figure 4.9 (a). The smallest size of the X-ray line foci (FWHM) is obtained at a distance (distance between RML array to the knife-edge) of 505 mm ± 19.5 mm, which gives the focal distance. This value is close to the theoretical value of 520 mm. In Figure 4.9(b), the evaluated size of line foci (FWHM) for 60 RMLs at the focal distance is presented. For each line foci, the recorded intensity as a function of the knife-edge position was differentiated and fitted by the Gaussian function, resulting in the average focal size of $\Delta_{diff} = 750 \pm 29$ nm (FWHM), which is consistent with the theoretical value $\Delta_{diff} = 736$ nm. By substituting the value of the focal distance in the eq. (2.18), the depth of focus of a single RML is 32 mm. The depth of field is 39 mm, according to eq. (2.19). Thus, the size of line foci formed by all RMLs was nearly constant in the depth of field.

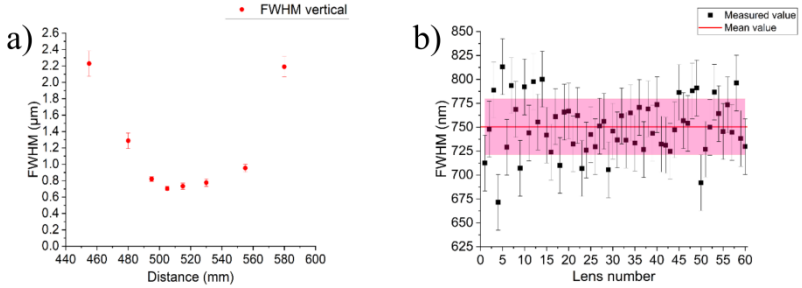

Figure 4.9: Focusing evaluation by the knife-edge scan with 100 nm steps. (a) The size of line foci (FWHM) vs. the distance of the knife-edge and RML array. The focal distance is 505 mm for 35 keV X rays. (b) The size of line foci (FWHM) for 60 RMLs at the focal distance. The average X-ray intensity line width is 750 ± 29 nm (vertical focus) [38].

The source point of most of synchrotron radiation sources has an elliptical shape. Generally, the vertical source size is much smaller than the horizontal one. As a consequence, the size of the generated X-ray intensity line (or spot) is smaller than the horizontal one. To study the influence of the source size on the focusing performance, the inclined RMLs were also characterized in the horizontal direction by rotating the inclined RMLs by 90^0. The experimental setup is presented in Figure 4.10.

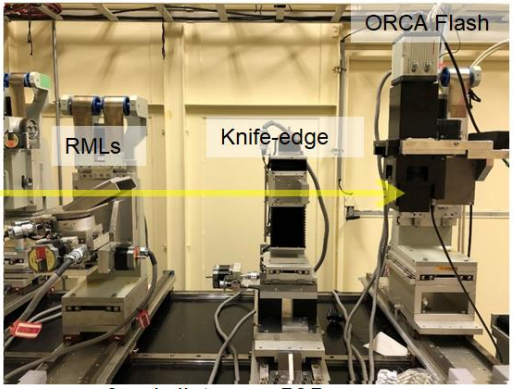

Figure 4.10: Picture of the experimental setup to determine the source size influence

The knife-edge scanning procedure was done in the same way, as it was performed concerning the vertical orientation. Since the focal distance does not depend on the orientation of the inclined RMLs, the measurements started from 505 mm, and then the knife-edge was moved upstream (up to 430 mm) and downstream (580 mm) the optical element. The measured size of the X-ray line foci width (FWHM) at the different positions of the knife-edge is presented in Figure 4.11.

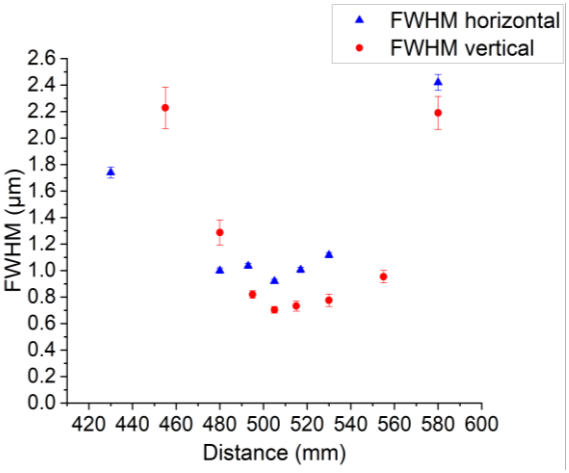

Figure 4.11: Influence of the source size on the size of line foci. The size of line foci (FWHM) in the vertical and horizontal direction vs. knife-edge position.

The smallest size of the line foci (FWHM) is at the focal distance 505 mm, which is similar to the one measured for the vertical orientation. As expected, the X-ray line's width is slightly larger than the vertical one; it is about 920 ±16 nm, due to the source size 150 µm (H) and 15 µm (V). Therefore, to demonstrate the highest possible spatial resolution of the PSR-STHXM, the inclined RMLs were oriented vertically. However, if larger FOV is preferable than spatial resolution, the inclined RMLs should be oriented horizontally. In this case, the FoV will be increased from 1.87×1.87 cm^2 to about 5×2.5 cm, since the number of lenses in one RML is 2000 (with 24 µm physical aperture) and the beam size at the sample position is 300 mm in the

horizontal direction. Furthermore, the camera with a larger number of pixels should be utilized.

4.3.1 Comparison of X-ray focusing properties with unpolished inclined RMLs.

Grounding and polishing the nickel structures is a critical step in fabricating the inclined metal structures and may lead to a structure damaging due to applied mechanical forces. Accordingly, from the fabrication point of view, this step should be avoided if the focusing properties are not influenced, especially in the transition zone. Therefore, the "unpolished" inclined RMLs (sample LFOV_4) were also characterized using the same conditions as the polished ones. The characterization has been done for the vertical orientation as described above. The knife-edge technique was performed with a 100 nm step. The comparison of the measured X-ray line foci width (FWHM) is presented in Figure 4.12.

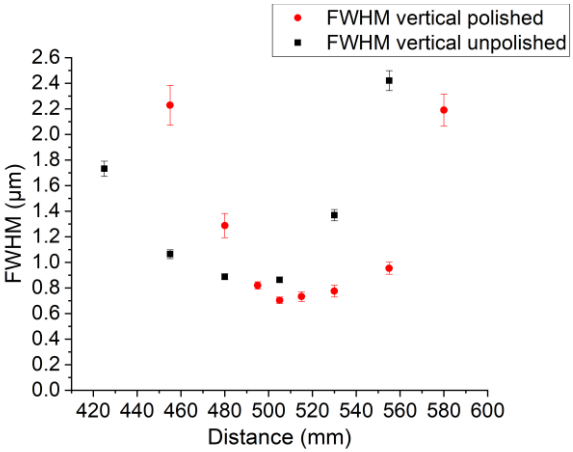

Figure 4.12: Comparison of the measured size of the X-ray line foci width for polished (LFOV_2) and unpolished (LFOV_4) inclined RMLs. The focal distance for both of them is 505 mm.

The size of the X-ray line foci (FWHM) at the focal distance are almost the same; the difference of about 100 nm is within the measurement error (the scanning step was 100 nm). This result proves that the grinding and polishing have no influence on the structure quality.

However, the unpolished surface of the inclined RMLs results in the different structure height in the range of 15 µm. Consequently, the effective height is significantly reduced, and the transition zone is larger than 3 pixels. Due to the X-rays scattering from the rough surface of nickel structures at the focal plane, some distortions of the wavefront were observed in the transition area (see Figure 4.13). Moreover, the transition area is not uniform; it is a drawback for PSR-STHXM. As a consequence, unpolished structures could not be used for imaging experiments.

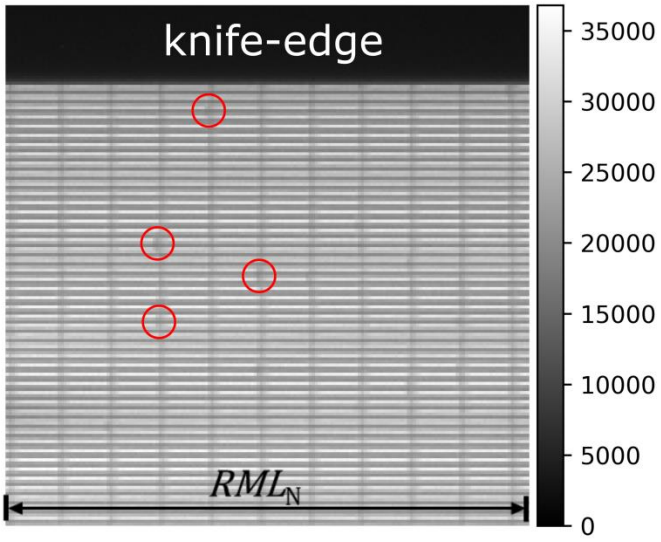

Figure 4.13: Image of the X-ray line foci size produced by the unpolished inclined RMLs. Wavefront distortions in the transition area are visible. Some of them indicated by red circles.

5 Pixel super-resolution scanning transmission hard X-ray microscopy

In this chapter, the pixel super-resolution scanning transmission hard X-ray microscopy(PSR-STHXM) is presented. The PSR-STHXM is a combination of the scanning transmission X-ray microscopy (STXM, described in the Theory chapter) and a pixel super-resolution (PSR) reconstruction technique. To avoid readers' confusion with the optical microscopy super-resolution techniques that provide spatial resolution beyond the diffraction limit, the term pixel super-resolution (PSR) is used [20]. PSR allows to reconstruct the super-resolution image from a set of sub-pixel low resolution (LR) images. The sub-pixel shifted LR images are achieved by scanning the sample through the measured X-ray foci and acquiring the LR images at each sample position. Consequently, the LR image contains the information of the sample only from the illuminated area. Therefore, the spatial resolution of the developed technique is equal to the measured diffraction-limited spot size and scanning step of the sample.

One of the main advantages is that PSR-STHXM provides a large FOV (mm-cm order) compared to other microscopy techniques while keeping the high resolution. It also gives a low scanning time.

The spatial resolution is a measure of the smallest object that can be resolved. Consequently, it is one of the fundamental parameters of any X-ray microscopy and imaging techniques. In this work, for 1D RML at 17 keV the spatial resolution of the PSR-STHXM was determined by imaging of a test resolution pattern. For the 2D CRMLs and staircase-array of inclined RMLs, the spatial resolution was estimated using the line spread function (LSF), which is a derivative of the edge spread function (imaging system response to a high contrast edge).

For all three techniques, scanning time was determined by the acquisition of low resolution (LR) images, which includes the exposure time per image, detector response, and the number of images. The number of LR images for PSR-STHXM is defined as a ratio of the space between micro (-nano) probes and the sample stepping value. According to the Nyquist Sampling Theorem [90], the sample scanning step was defined as half of the measured X-ray foci size (FWHM), as shown in Figure 5.1. The sample movement was performed within the distance between neighboring foci. In scanning microscopy techniques, the precise stepping of the sample is the crucial parameter. Any vibrations or imprecision of the movement system reduce the spatial resolution and cause image artifacts. Hence, during the PSR-STHXM experiments, the scanning was performed by using a piezo motor or goniometer.

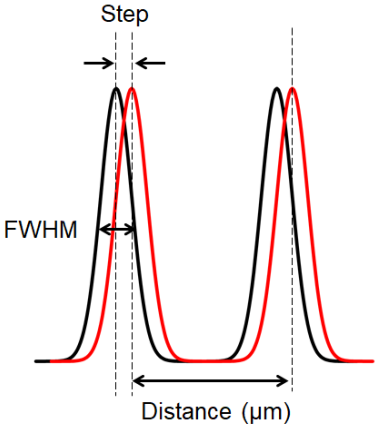

Figure 5.1: Illustration of the sample scanning procedure. The scanning step is defined by the measured size of the X-ray line foci (FWHM)—the initial position of the sample (black) and the sample shift with a step of FWHM/2. The sample scanning is done within the distance between the adjacent X-ray foci.

The PSR-STHXM was performed using the following procedure:

1. Placing the sample to be studied in the focal plane.
2. Acquisition and normalization of m×n images at each sample scanning position through the intensity of the X-ray line (or point) foci

3. PSR image reconstruction
4. Spatial resolution evaluation

In the following sections, the working principles of PSR-STHXM by using the 1D and 2D X-ray optical elements, experimental setups, pixel super-resolution image reconstruction, imaging experiments, and spatial resolution improvement are presented. Moreover, the potential application of the developed technique for material science, such as X-ray microscopy of a dental implant abutment, is demonstrated.

5.1 1D PSR-STHXM

The pixel super-resolution X-ray imaging principle is shown in Figure 5.2. 1D RML is placed in the synchrotron beam and oriented vertically, expecting a high focusing performance. A monochromatic X-ray beam illuminates the 1D RML, and an array of line focuses is formed with a period equal to the imaging pixel period. The sample is placed in the lens array's focal plane and scanned through the X-ray line foci. The imaging detector is placed as close as possible to the sample, to avoid image blurring due to X-ray scattering and finite source size. According to the Nyquist sampling theorem, sample scanning is done using a sub-pixel step defined by the illumination spot's size as mentioned above. At each sample scan position, the generated X-ray microprobes illuminate the sample, and the information is stored in LR image pixels (Figure 5.2b). The number of LR images (N_{LR}) for PSR-STHXM technique is defined as a ratio of the space between microprobes (period of the lens array, P_{RML}) and the stepping value ($Step_{Piezo}$): $N_{LR}= \frac{P_{LA}}{Step_{Piezo}}$. The absorption image is defined by the ratio of the number of photons impinging on the LR pixel with and without the sample.

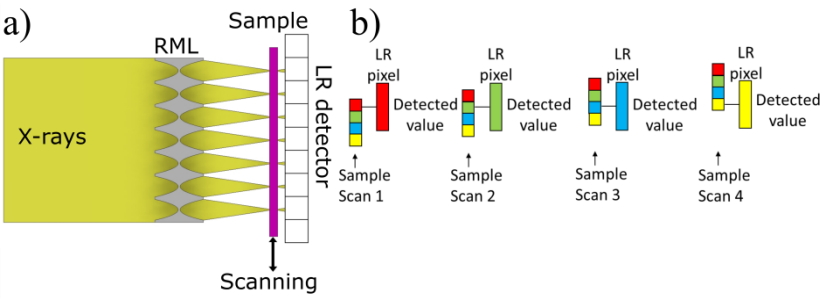

Figure 5.2: Representation of the PSR-STHXM technique. (a) X-ray imaging setup by using 1D RML for X-ray absorption-contrast imaging. (b) Formation of sub-pixel shifted LR images: at each sample scan position, the X-ray line foci illuminate the sample. The information about local transmission is measured by LR pixels at each sample position (indicated by different colors) [36].

As explained previously, from a set of sub-pixel shifted LR images, it is possible to reconstruct the pixel super-resolution (PSR) image with the spatial resolution equal to the X-ray line width (FWHM) while keeping the large FoV. Consequently, PSR image reconstruction [35] was performed according to the following model: the intensity $I_0(x,y)$, generated by the 1D RML, is recorded by the low-resolution detector, where x and y are the pixel coordinates with a pixel size of d. Scanning a sample through the focused beams in a vertical direction (y) with N steps leads to an intensity change $I(x,y)$ in the detector plane due to absorption by the sample. The sample scanning should be performed within one low-resolution detector pixel; therefore, the PSR resolution absorption contrast image $A_{SR}(x, Ny+n)$ is created as:

$$A_{SR}(x, Ny+n) = \frac{I(x,y)}{I_0(x,y)} \cdot \left(S\left(x = d, \frac{n \cdot d}{N}\right)\right), \qquad (5.1)$$

n represents the step number; therefore, n= 1…N, and $S\left(d, \frac{n \cdot d}{N}\right)$ is the scanning of the sample in the vertical direction y. The image is represented in a matrix form. Hence, PSR reconstruction is performed by sorting the row vectors of the recorded LR images with a pixel size of d/N and stacking them into the high-resolution grid as it is described in Figure 5.3.

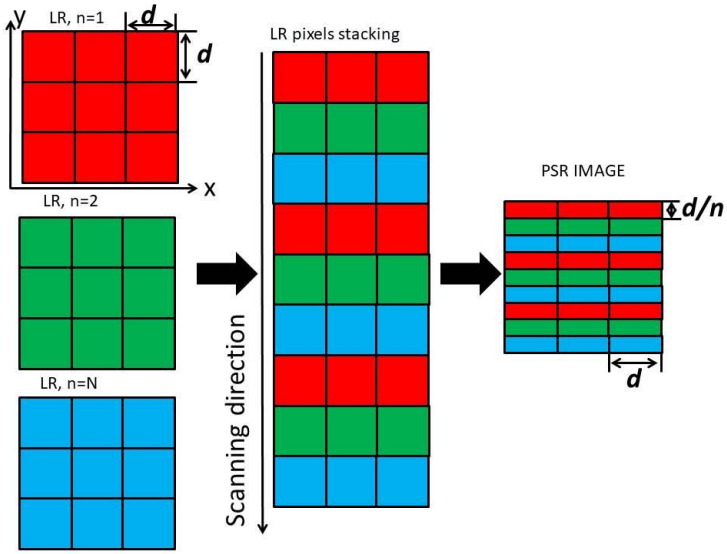

Figure 5.3: 1D PSR image reconstruction from a set of sub-pixel shifted LR images.

It should be noted that the spatial resolution is improved only in the scanning direction by using 1D RMLs. It stays unchanged in the perpendicular direction and equals to at least 2 LR pixels with the size *d* according to the Nyquist sampling theorem.

5.1.1 Proof of concept demonstration of 1D PSR-STHXM at 17 keV

The proof of concept demonstration was performed directly after the X-ray characterization of the 1D RML using the 17 keV X-rays (see Chapter 4). According to the X-ray line foci analysis, the potential FoV is 2.5 mm in the sample scanning direction (250 line foci with a period of 10 µm) and a length of X-ray line focus of 60 µm.

A triangular test pattern with a feature size of about 20 µm (in the scanning direction) × 50 µm, which can be studied within the FoV, was used. The triangular shape of the test pattern is perfect for developing a reconstruction

algorithm since it immediately shows the spatial resolution improvement. The test pattern was fabricated at IMT/KIT using e-beam lithography. SEM images of the triangular structures are presented in Figure 5.4. The triangular gold structures with 3 ± 0.5 µm height are on a 2 µm thick titanium membrane. The titanium membrane is nearly transparent for 17 keV X-rays, while the gold structure absorbs 51% of the X-rays. The membrane was fixed on an aluminum frame to keep it flat.

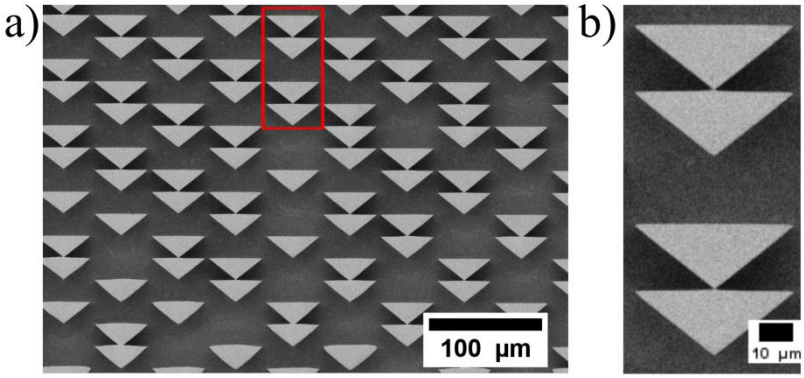

Figure 5.4: The triangular structures used for the development of the reconstruction algorithm.

The test pattern was placed at the focal distance of 67 mm downstream of the 1D RML. The detector was placed 1 cm behind the sample, which was the nearest suitable position not to hurt the detector. Sample scanning using a piezo stage (Physical Instruments, Germany) was performed with 1 µm steps within 10 µm. Consequently, 10 HR images were acquired by the detector with a pixel size of 0.65×0.65 µm^2. The exposure time was 10 s to acquire one good HR image due to low photon flux. The number of images is 10 since the distance between neighboring foci is 10 µm. The total scanning time was defined by the images acquisition duration with and without sample; it corresponded to approx. 4 min (ten HR images with sample 100 s, ten HR images without sample 100 s, sample stepping ca. 50 s). One of the HR images (1608×2154 pixels) is presented in Figure 5.5 (a). The black region

of the image (a) corresponds to the silicon substrate which absorbs the incoming X-ray beam. The 1D RML was oriented vertically, so producing the periodically spaced horizontal X-ray line foci. The white horizontal lines correspond to the X-ray line foci. As shown in Figure 5.5 (b), the triangular test pattern perfectly fits the FoV of the imaging setup.

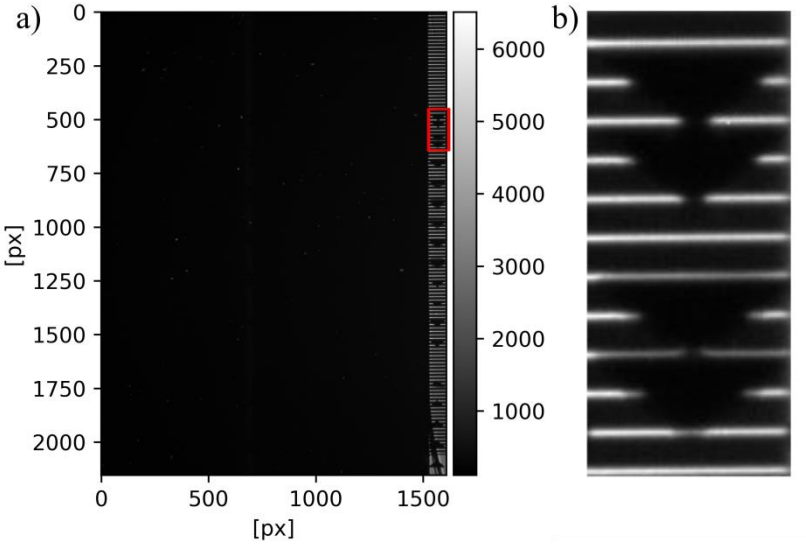

Figure 5.5: HR image of the triangular test pattern within the FOV.(a) Overview (b) ROI image of the triangular test pattern corresponding to the red box in (a) used for reconstruction.

Figure 5.6 shows the image processing for the PSR image reconstruction. First, a region of interest (ROI) image with 208 × 80 pixels was chosen to study the reconstruction process (Figure 5.6 a). ROI includes four triangles. As the next step, the HR raw images were flat-field, and dark-field corrected to obtain the normalized image (Figure 5.6 b). Finally, LR images with a pixel size of 10.4 µm × 1 µm were generated by 16 × 1 pixel binning of HR images in the scanning direction (Figure 5.6 c). Pixel binning and alignment were done using Numpy and SciKit image packages in Python programming language. The pixel binning was done to make a proof of concept and pre-

sents what will be seen by using a detector with LR pixels (10 µm in our case).

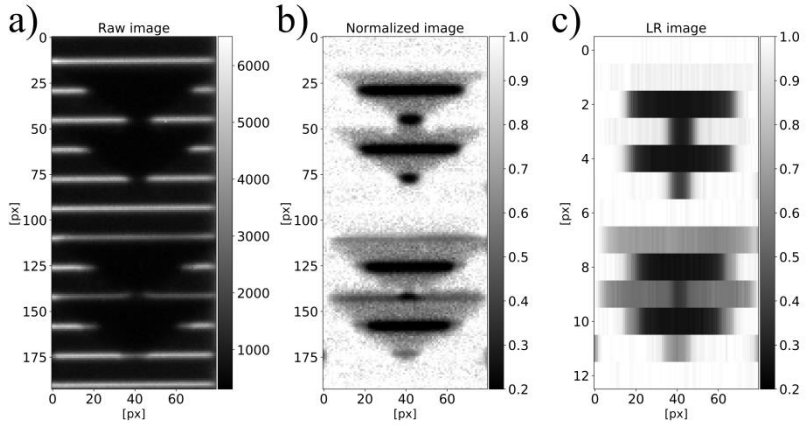

Figure 5.6: Image processing for PSR reconstruction: recorded ROI of HR image (left), the normalized image (mid), and LR image obtained by 16 × 1 pixel binning of the HR image.

The same procedure was performed for all 10 HR images. As a result, we obtained a set of LR images. The ROI 10 LR images of a triangular test pattern with a 1 µm sub-pixel shift were used for 1D PSR reconstruction. Each LR image has a size of 13 × 80 pixels (pixel size 10.4 µm ×80 µm). Figure 5.7 demonstrates the image formation during the test pattern scanning through X-ray line foci. It is clearly visible how the information is stored in the LR detector pixels. It should be mentioned that for a successful PSR reconstruction, each intensity line should be aligned in the center of the corresponding pixel. Besides, only one X-ray line should hit the pixel. Otherwise, if two (or more) intensity lines illuminate one pixel, the sample's information from both of them will be registered, and PSR reconstruction will not work. In our case, only one intensity line illuminated the sample in one pixel. Therefore, we successfully obtained the PSR image by using our reconstruction algorithm (described earlier in section 5.1).

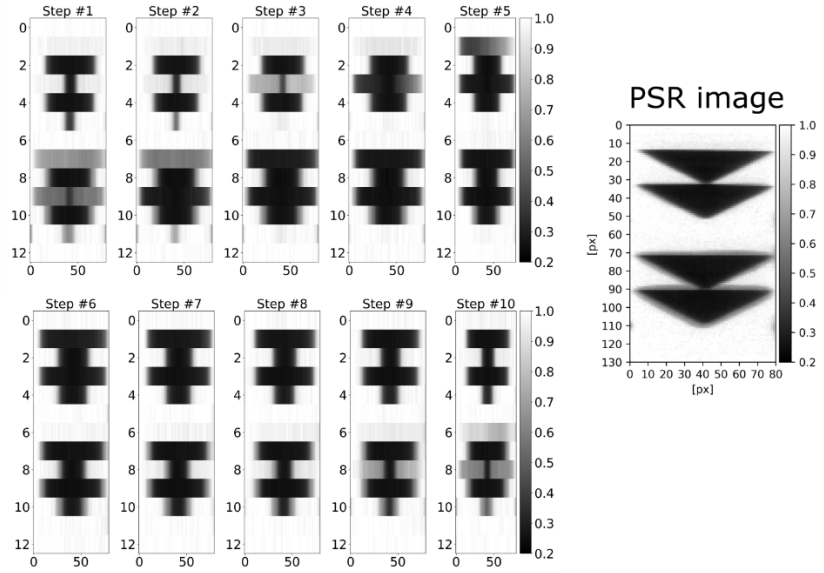

Figure 5.7: Pixel super-resolution reconstruction image of the triangular test pattern from 10 LR images (pixel size 10.4 × 0.65 μm). The PSR image has a pixel size of 1.04 μm × 0.65 μm.

5.1.2 The spatial resolution of PSR-STHXM by using 1D RML.

Since PSR-STHXM with a 1D RML is sensitive in only one dimension, a 1D resolution test pattern (lines and space) was used for the spatial resolution quantification. The resolution test pattern was on the same titanium membrane, near the triangular test pattern. SEM images are shown in Figure 5.8

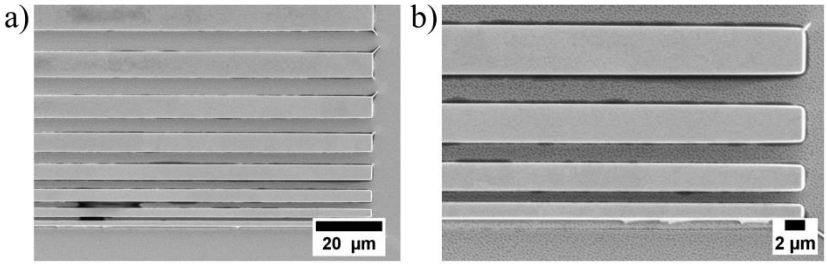

Figure 5.8: The thickness of gold structures is similar to the triangular ones, (3 ± 0.5 µm); they have a length of 1 mm. The smallest line width was about 1.5 µm.

PSR-STHXM was performed using the same experimental setup and imaging conditions as for the triangular structures described above. In total, 10 HR images were registered by the detector, and afterward, flat-field and dark-field corrected. In contrast to the triangular test pattern, it is possible to demonstrate how the "real" detector forms the image using a line and space test resolution pattern. The standard X-ray imaging detectors have a rectangular pixel size. Therefore, the LR images with a pixel size of 10.4 µm × 10.4 µm were generated by 16 × 16 pixels 2D binning of HR images. A set of sub-pixel shifted ROI LR images with an image size of 15 × 5 pixels is shown in Figure 5.9. Consequently, the ROI image is 156 µm in the scanning direction and 52 µm in the perpendicular direction.

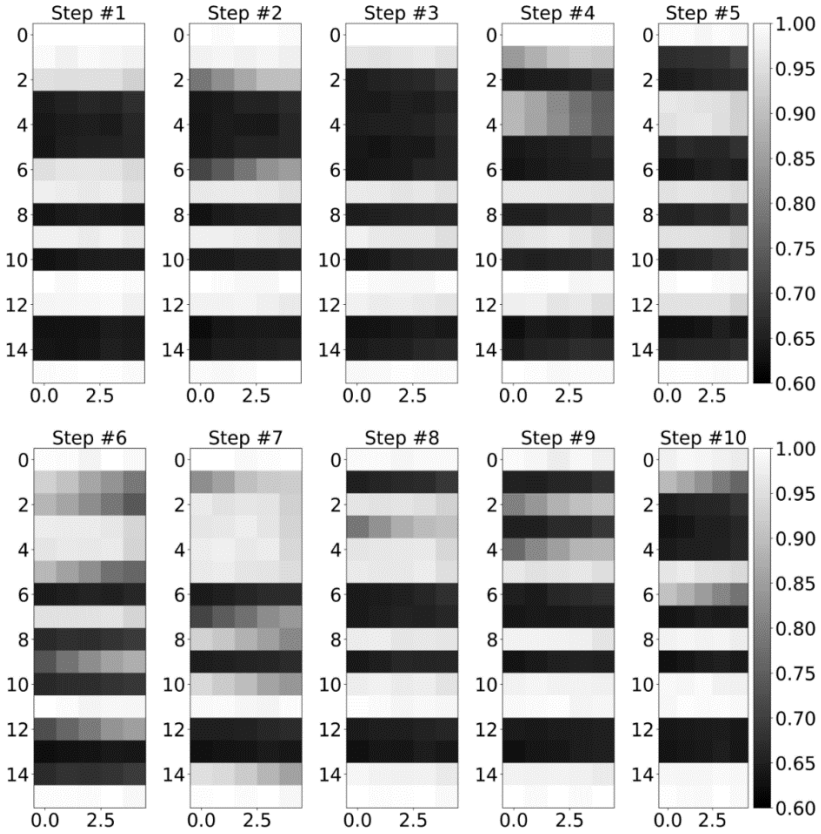

Figure 5.9: Image formation in the 1D PSR-STHXM by using a test resolution pattern. The LR image consists of 15 × 5 pixels.

Next, the PSR reconstruction was performed. The achieved PSR image of the resolution test pattern and the comparison with the LR image and HR image is presented in Figure 5.10.

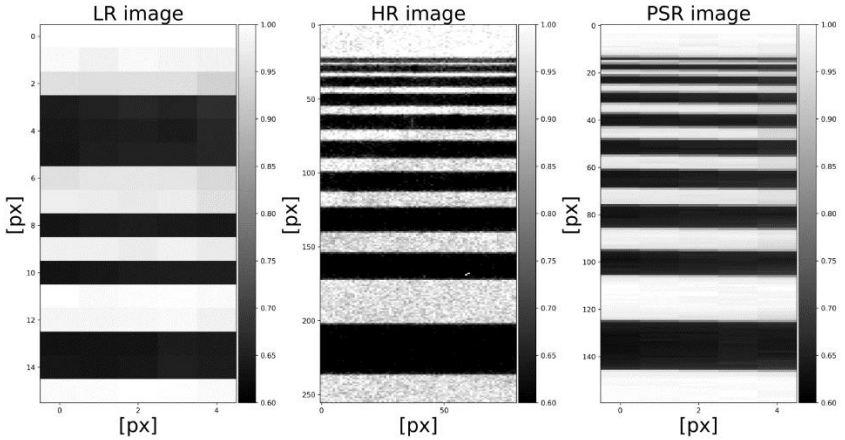

Figure 5.10: PSR-STHXM of a resolution test pattern: (a) LR image (pixel size: 10.4 µm) formed from an HR image by 2D binning, (b) HR image (pixel size: 0.65 µm) as measured. (c) Reconstructed PSR image (pixel size: 1.04 µm) from ten LR images.

As seen in the PSR image, the smallest feature of 1.5 µm was resolved. Therefore, the spatial resolution of PSR-STHXM using 17 keV X-rays is at least 1.5 µm. Moreover, the PSR image is less noisy than the HR image since it was reconstructed from ten LR images (more statistics). The spatial resolution is improved in the scanning direction by a factor of 7 using the detector with a pixel size of 10 µm. The FoV was 2.5 mm × 60 µm limited by the height of the 1D RML. The scanning time was 4 minutes at the IMAGE beamline/KARA synchrotron facility. It can be improved by performing PSR-STHXM at the synchrotron facilities with higher brilliance (photon flux). The potential application of the 1D PSR-STHXM is the investigation of micro (-nano) wires, X-ray gratings with long lamella design, etc.

Since the presented imaging technique is sensitive in the one (scanning) direction only, a 2D PSR-STHXM was developed. The aim is the spatial resolution improvement in 2D by merely scanning the sample in 2D without the need to rotate the sample by 90^0.

5.2 2D PSR-STHXM using 2D Compound RMLs at 34 keV

2D sub-pixel resolution scanning transmission X-ray imaging is a straight forward extension of the one-dimensional method described in [36]and is shown in Figure 5.11. The point foci with an intensity $I_0(x, y)$ created by the 2D CRMLs, are recorded by a Medipix Merlin 3.0 photon-counting detector. The region of interest of the Medipix detector was chosen to be 34 × 34 pixels corresponding to the geometrical size of the 2D CRMLs (1.87×1.87 mm^2) (described in chapters 3 and 4). The CRMLs are positioned in the beam and aligned parallel to the detector by rotating the optics around the optical axis. It is parallel when a detector pixels row switches from completely dark to fully illuminated when shifting the foci of the 2D CRMLs over the border between pixels in the vertical direction. In the same way, a column of foci is positioned above the border between detector pixels by moving the foci of the 2D multi-lens array over the detector pixels in a horizontal direction. From that position of the CRMLs, the point foci are centered on the detector pixels by shifting them by half a pixel pitch in vertical and in the horizontal direction. The size of the point foci is much smaller than the pixel size $p = 55$ µm. So each focus point illuminates only one pixel.

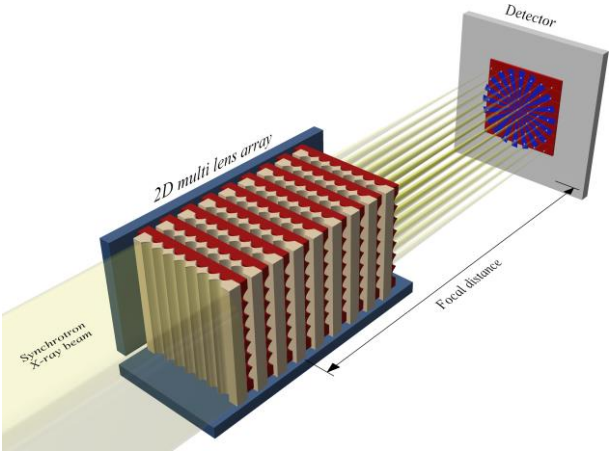

Figure 5.11: Principle of 2D PSR-STHXM. The Siemens star is placed in the focal plane. At each sample position, the intensity variations are recorded by a low resolution (LR) detector (Medipix in this work), which is placed as near as possible behind the Siemens star. The physical aperture of the individual CRMLs matches the pixel size. Each point foci hits its corresponding pixel in the center. 2D PSR-STHXM has achieved by raster-scanning the sample with sub-pixel sized steps through the point foci [37].

The 2D PSR reconstruction is done according to the following model (extension of the 1D PSR reconstruction):

$$A_{\mathrm{SR}}(Mx+m, Ny+n) = \frac{I(x,y)}{I_0(x,y)}\left[S\left(\frac{m\times d}{M}, \frac{n\times d}{N}\right)\right], \tag{5.2}$$

Incident X-ray point focus intensity $I_0(x,y)$ generated by the 2D CRMLs, intensity variation due to the absorption by the sample $I(x,y)$; m, n represent the step number, therefore $m = 1\ldots M$ and $n = 1\ldots N$ and $S\left(\frac{m\times d}{M}, \frac{n\times d}{N}\right)$ gives the number of the pixels in x- and y-direction [35][36].

For a better understanding of the image formation, we have performed sparse scanning of the sample; it was scanned in the vertical and horizontal directions without a raster scan. After the X-ray characterization, the sample was

placed at the focal distance, and the Medipix detector replaced the high-resolution indirect detector.

5.2.1 2D PSR-STHXM image reconstruction

As a test pattern, we used a Siemens star that was in-house fabricated using deep X-ray lithography and electroplating. Figure 5.12 shows the SEM image of the Siemens star with still some remaining resist (resist partially stripped) which protects the gold structures from collapsing. The test pattern consists of a 1 mm thick polyimide substrate (Vespel SEK–3000, DuPont) with a gold structure of (110 ± 0.5) µm thickness on top. The polyimide substrate is nearly transparent for 34 keV X-rays (transmission ca. 96 %), whereas the gold structure absorbs 98 % of the X-rays.

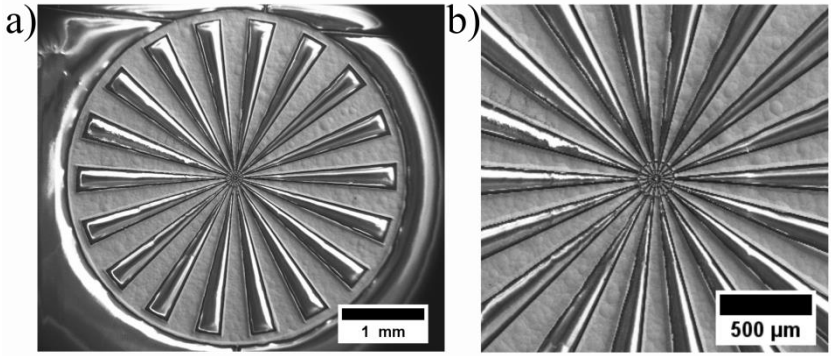

Figure 5.12: SEM image of the resolution test pattern used for 34 keV PSR-STHXM (left) and Zoom – in view, image size:1.87 × 1.87 mm and equals the size of the 2D CRMLs. The smallest feature size at the end of the arrows is approx. 2 µm.

For the proof of principle 2D PSR-STHXM, a Medipix Merlin 3.0 photon-counting detector (FoV 14 mm x 14 mm, 256 × 256 pixels, 55 µm pixel size, CERN, Geneva, Switzerland) was used working in Charge Summing Mode (CSM). In Figure 5.13, the X-ray radiography image of the Siemens star registered by the Medipix detector is presented. The sample was positioned at 349 mm from the entrance aperture and 12 mm in front of the detector.

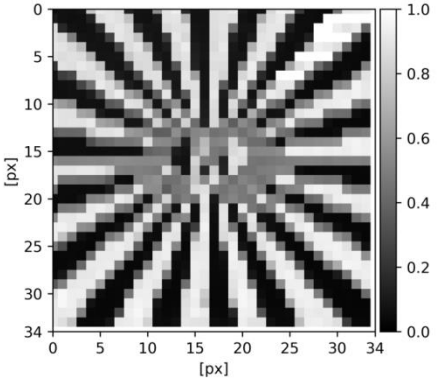

Figure 5.13: Acquired image by the Medipix detector. The region of interest (ROI) of a Siemens star is 34 × 34 pixels (pixel size is 55×55µm) corresponding to the geometrical size of the 2D CRMLs [37].

As shown in Figure 5.13, the region of interest (ROI) of the Medipix detector is 34 × 34 pixels corresponding to the geometrical size of the 2D CRMLs. The ROI where the Siemens star is visible was chosen for the 2D PSR-STHXM. Also, the LR image contains artefacts (white pixels) due to radiation damage (which is a result of the high concentration of intensity produced by the 2D CRMLs) of the electronics, which resulted in the residual signal from some pixels which remained for some time after switching of the X-ray beam. However, during the beamtime, there was no option to change sensor material to Cadmium telluride (CdTe), which is used for high energy X-rays (above 30 keV). Therefore, to avoid detector damage (especially electronics) due to high charge concentration in a small pixel area, a 3 mm Al-filter (X-ray absorption is ca. 50% at 34 keV) had to be placed in the beam to reduce the intensity. This significantly increased the exposure time per image to 1 s.

Sample scanning was performed using a piezo stage (Attocube ECSx5050 nanopositioner, Haar, Germany) with 1 µm steps within the 55 µm pixel size. At each sample step, one LR image was acquired with an exposure time of 1 s (Figure 5.13). Scanning one line (vertical or horizontal) took about 5 min: 110 s exposure time for 55 LR images plus 55 images without a sample in the

beam plus 170 s for sample moving and overhead times. Due to beam time constraints at Diamond B16, only two line scans could be performed, one in vertical and one in a horizontal direction instead of a full raster scan.

PSR image reconstruction model described before was performed. All X-ray images were flat field and dark field corrected. Then, the CRMLs region corresponding to the 34 × 34 pixels was cropped from the ROI 80 × 80 pixels LR image. Each LR image consists of the sub–pixel information corresponding to the half of the intensity spot size in vertical direction and a scanning step, in this case, equal to 1 μm. In Figure 5.14(a) and Figure 5.14(b), sub–pixel image formation owing to the sparse scanning within 55 μm pixel size of the Siemens star using Medipix detector in the horizontal and vertical direction is presented. Black pixels correspond to the missing values during the sparse scanning.

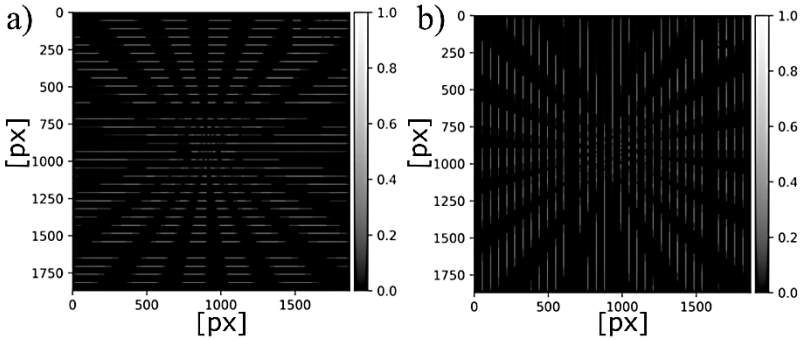

Figure 5.14: 1D sub-pixel image formation relative to the sparse sample scanning in horizontal (a) and vertical (b) direction. The images were reconstructed with a size of 1870 × 1870 pixels (1 pixel is 1 μm)

Figure 5.15 shows the sub-pixel image of the Siemens star obtained from the two line scans performed. The information of the smallest features with the size of 2 μm of the specimen is visible in the center of the PSR image. The artifact in the upper right corner results from erroneous signals of the detector. These could not be avoided in the actual measurement as their location

changed. Black pixels in between the bright lines correspond to missing values due to the sparse scanning.

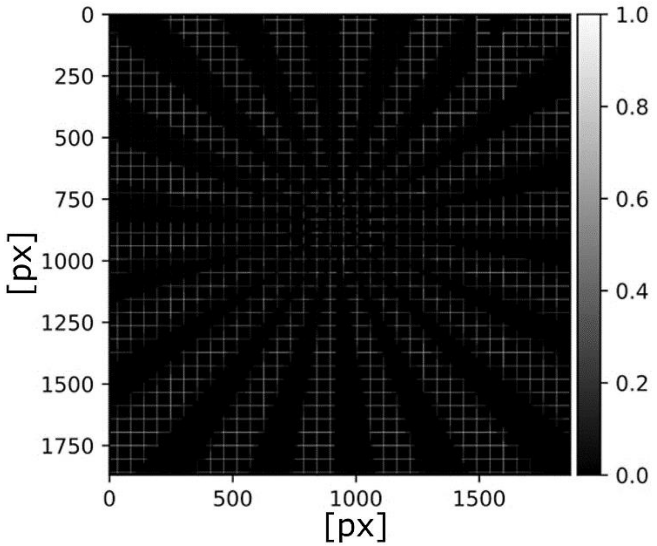

Figure 5.15: The proof of concept of 2D PSR image formation of a Siemens star, including only one horizontal and one vertical line sample scanning with the sub-pixel shift. Reconstructed 2D PSR image (step size: 1 µm), which is a sum of the vertical and horizontal 1D sub-pixel resolution images [37].

It should be noticed that the scanning time for a complete raster-scan would be in the range of ca. 50 minutes. Nevertheless, it is still much faster, under comparable conditions, than the conventional single probe STXM. A complete raster-scan of the Siemens star within the area equal to the 55 µm pixel size would give a complete 3.5 megapixel 2D sub-pixel resolution image with 1870 px ×1870 px.

5.2.1 The spatial resolution of PSR-STHXM by using 2D CRMLs.

The spatial resolution of the 2D PSR-STHXM can be evaluated separately from the PSR images. To do so, the 1D PSR reconstruction was performed for both scanning directions from the LR images (80 × 80 pixels which corresponds to one chip of the Medipix detector) without cropping the ROI. The resulting PSR images (see Figure 5.16) demonstrate significant improvement of the spatial resolution in the scanning direction for the area corresponding to the 2D CRMLs size, shown in Figure 5.13. Simultaneously, the comparison with the PSR image without the optics can be seen.

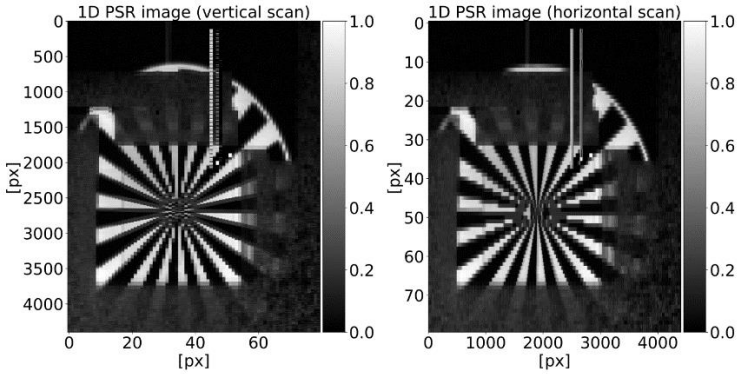

Figure 5.16: 1D PSR images of the Siemens start in sample scanning directions reconstructed from 55 LR images. The PSR image size is 4400 × 80 and 80 × 4400, respectively.

The spatial resolution in the scanning directions was determined from the line spread functions (see Figure 5.17). It is 2 µm (vertical) × 2.5 µm (horiz.), respectively. The spatial resolution entirely coincides with the size of point foci, which is 2 µm (v) × 3 µm (h).

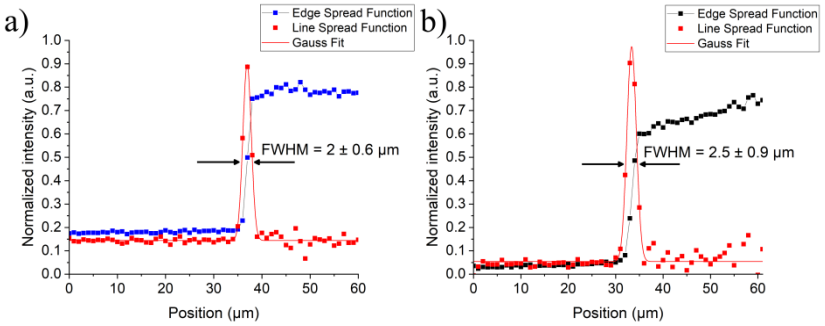

Figure 5.17: The spatial resolution of the 2D PSR-STHXM was calculated from ESF and LSF. a) for the vertical scanning direction b) for the horizontal one.

The 2D PSR-STHXM using the Medipix detector (55 µm pixel size) and 2D CRMLs allowed to improve the spatial resolution by a factor of about 25 in a FOV of 1.87×1.87 mm^2, which was the fabrication limit of DXL (deep X-ray Lithography).

5.3 Large FoV PSR-STHXM using the staircase-array of inclined RMLs at 35 keV

To overcome the limitations mentioned above and finally reach the thesis goal: sub-µm spatial resolution, FoV in the cm range, only several minutes scanning time, and using hard X-rays (35 keV), a large FoV PSR-STHXM based on the staircase-array of inclined RMLs, was developed.

The concept of large FoV PSR-STHXM is shown in Figure 5.18. Similar to the 1D PSR-STXHM using a single 1D RML, illuminated by monochromatic plane-wave X-rays, a staircase array of inclined RMLs generates periodically spaced X-ray line foci with a spacing between neighboring foci equal to the period of the lenses and equal to the virtual detector pixel size. The sample is placed in the focal distance and scanned through a large number of X-ray focus lines with step sizes slightly below the size of the X-ray focus line

(FWHM). At each sample scanning position, a LR X-ray image is recorded. Then, the HR image is reconstructed from a set of sub-pixel shifted LR images by the PSR reconstruction algorithm.

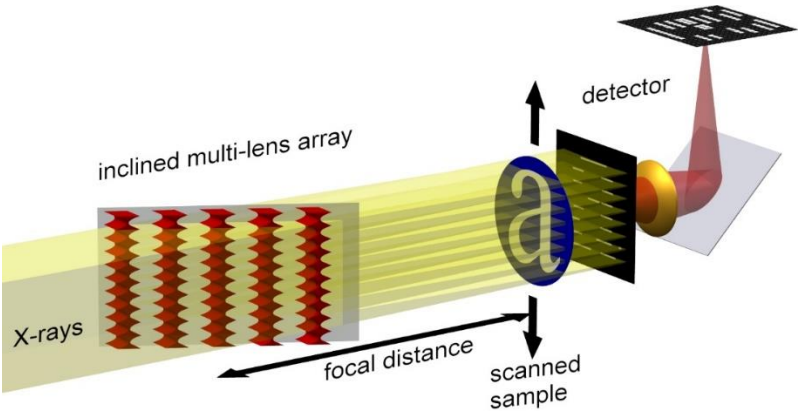

Figure 5.18: Concept of the large FoV PSR-STHXM based on the inclined multi-lens array. The substrate is tilted with respect to the incoming X-ray beam. Therefore, all of the inclined RMLs oriented in a staircase arrangement, resulting in a cm long X-ray line foci. The sample is placed in the focal distance and scanned through the line foci [38].

5.3.1 The spatial resolution of large FoV PSR-STHXM by using the staircase array of inclined RMLs

The spatial resolution was determined by using a lead X-ray test chart ("Type 14", Moriyama X-ray Equipments Co., Ltd) . The transmission through the test chart pattern was 50.2 % at 35 keV. The test chart's geometric size is 35×25 mm^2, with the smallest feature of 20 line pairs per mm (25 μm lines and 25 μm space).

The test chart was placed at 505 mm (focal distance) downstream of the inclined RMLs. It was scanned with a 300 nm step size with an exposure time of 1.5 s at each step. Since the spacing between adjacent X-ray line foci was 24 μm, the specimen was scanned within 24 μm, resulting in 80 images. The

total exposure time was 2 minutes, and including the dwell time of about 2 minutes, the total scanning time was 4 minutes. For the PSR reconstruction, the recorded image pixels (pixel size 8.03 × 8.03 μm^2, number of pixels 2048 × 2048) were 3 × 1 binned in the sample scanning direction for obtaining LR images with the size of the pixels of 24.09 μm × 8.03 μm and the corresponding number of pixels was 682 × 2048. The 1D PSR reconstruction was performed. In Figure 5.19 (a), PSR image of the resolution test chart pattern is presented. The PSR image size is 54560 × 2048 pixels with a pixel size of 300 nm × 8.03 μm giving the FoV of 1.64 cm × 1.64 cm. The spatial resolution was defined from the line spread function, which is the derivative of the edge spread function shown in Figure 5.19 (b) and (c). Therefore, the spatial resolution in the scanning direction is 780 nm ± 40 nm, which is equal to the X-ray focal width, and the spatial resolution in the perpendicular direction was 20.4 ± 1.05 μm due to the fact that there is no focusing in vertical direction.

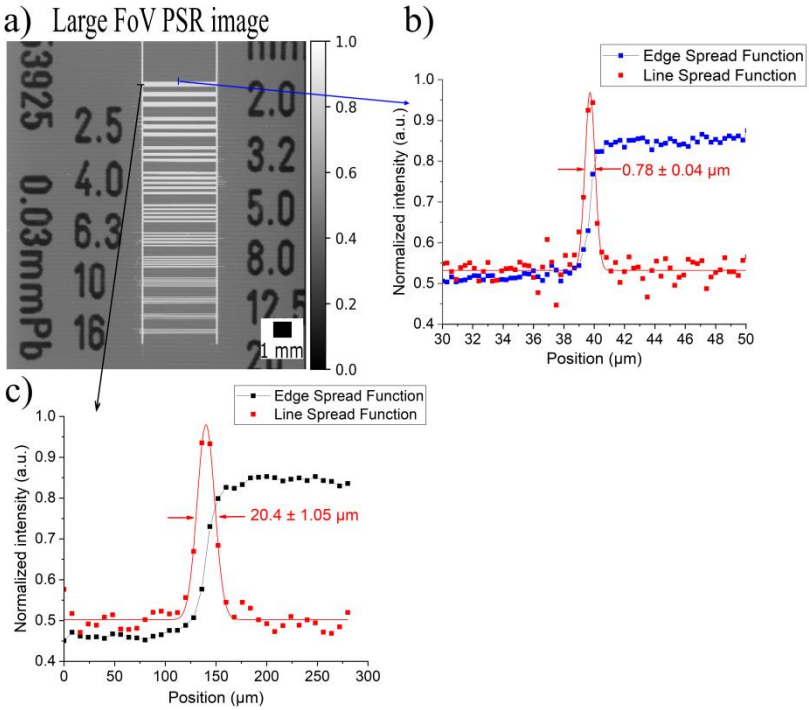

Figure 5.19: Spatial resolution of a large FoV PSR images (a) (pixel size 300 nm × 8.03 µm). The image size is 1.64 × 1.64 cm^2. Spatial resolution in the scanning direction is 780 nm ± 40 nm (b), and (c) in the perpendicular direction is 20.4 ± 1.05 µm (FWHM) [38].

For a demonstration of the advantage of the PSR microscopy technique, a comparison of the zoom-in view (boxes blue and red in Figure 5.20) with the optical microscopy images and LR images of the same area is presented. It was found that the smallest features (25 µm line and space), defects and cracks, caused by the manufacturing process are resolved in the PSR images as in optical microscopy images, which are not resolved in LR images.

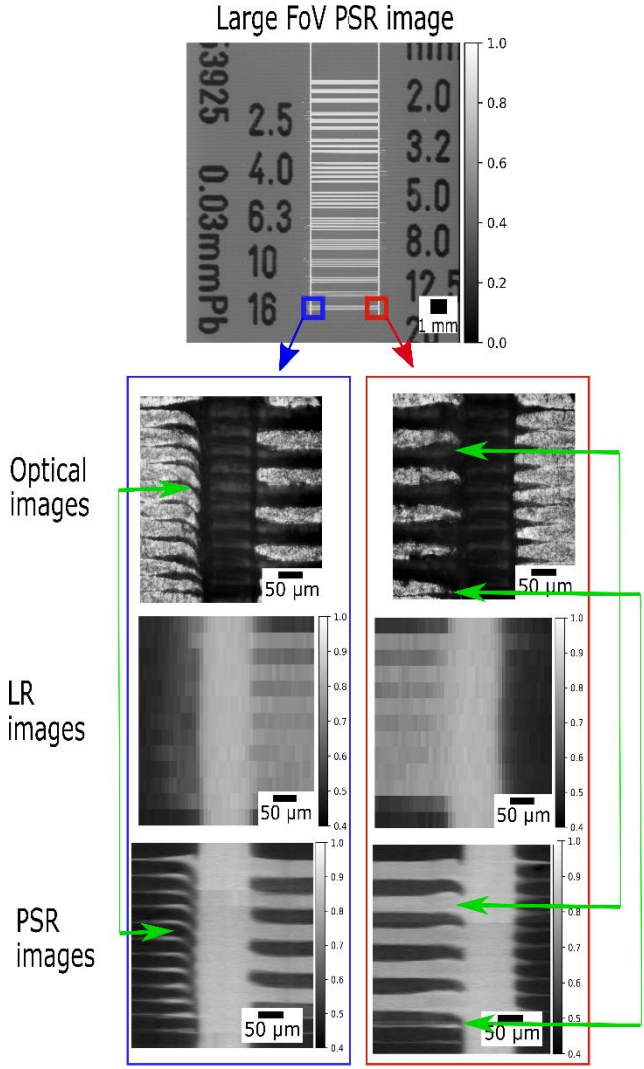

Figure 5.20: Comparison of the optical microscopy, low-resolution (LR) (pixel size 24.09 µm × 8.03 µm), and PSR-STHXM images of the resolution test pattern: The smallest features (25 µm line and 25 µm space) and some defects and cracks are resolved in PSR-STHXM images, as indicated by the green arrows.

5.3.2 Application of large FoV PSR-STHXM for studying extended and thick specimens

As a possible application of this new method, 3D printed parts from a dental implant system were analysed. The so-called dental implant abutment represents the middle section of a modern state of the art three-part dental implant system, connecting the visible prosthesis (crown) to the bone screw (implant). The abutments are fixed to the lower implant with a small screw, and the upper prosthesis is cemented on to the abutment with a dental composite. The abutments were 3D printed by Selective Laser Melting (SLM) technology out of the medical-grade material powder Ti6Al4V ELI (Titanium Gr. 23) [92]. Figure 5.21 (a) shows the part after SLM fabrication and shows the typical rough surface resulting from SLM manufacturing. The support structures to the base plate can also be seen. Figure 5.21 (b) shows the implant abutment part, which has been finalized by additionally mechanical preparation to result in final tolerances, desired surface qualities, and additional features like the implant-abutment connection interface. The parts' production via 3D printing and machining can be monitored with the X-ray technique to ensure quality relevant parameters and further recognize cracks or holes inside the material.

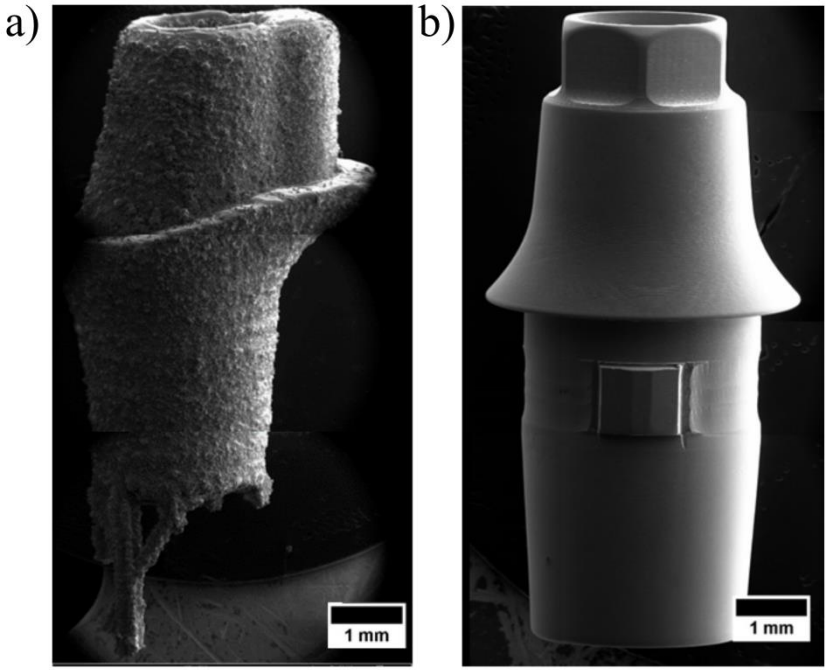

Figure 5.21: Samples for the application: 3D printed dental abutment made of Ti-6Al-4V ELI (a) and finished one (b).

In Figure 5.22, a comparison between a PSR image and a conventional X-ray radiography (pixel size $8.03 \times 8.03\ \mu m^2$) is shown. The scanning procedure for large FoV PSR-STHXM of the abutment was exactly the same as that used for the X-ray test chart pattern (Figure 5.19). Simply, the test resolution pattern was replaced by the dental abutment. The zoom-in view of the internal thread in the PSR image is sharper than the conventional ones, indicating the image contrast enhancement. Also, the pitch and the width of the thread are more visible due to 300 nm pixel size. Therefore, PSR-STHXM provides a large FoV as in conventional X-ray radiography setup and high spatial resolution as in STHXM. Moreover, it allows the investigation of the full implant abutment which is not possible by a single X-ray nanoprobe.

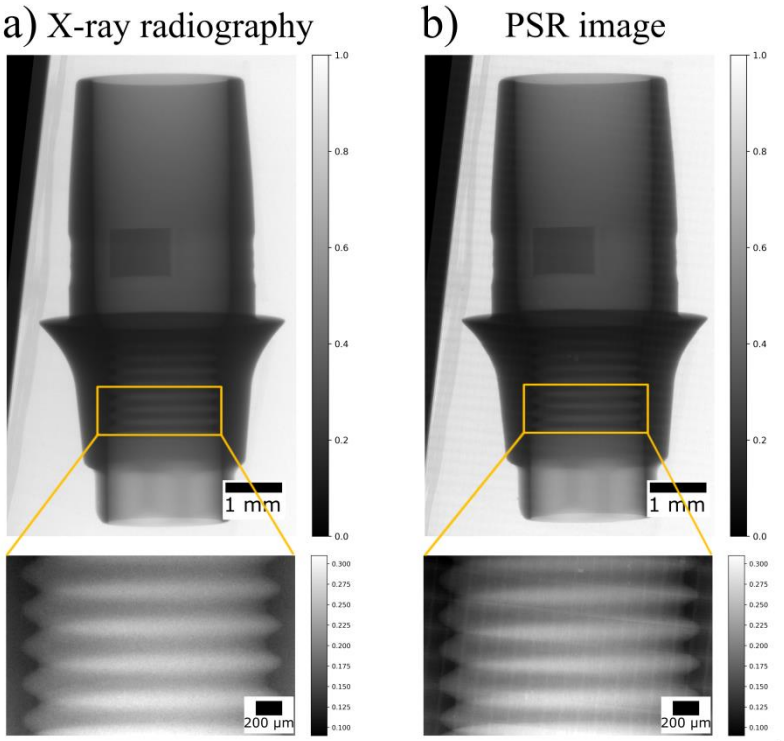

Figure 5.22: Application of the large FOV PSR-STHXM for investigating biomedical implants with the zoom-in view of the internal thread fabricated via selective laser melting and comparison with conventional X-ray radiography image (a) (pixel size $8.03 \times 8.03\ \mu m^2$) [38]

Large FoV PSR-STHXM is a useful tool for characterizing biomedical implants at 35 keV, even in the X-ray radiography mode. In the future, it is possible to perform computed tomography studies of these specimens in three dimensions allowing to analyze in detail the surface roughness, deviation from the CAD design, possible cracks, or defects caused by the selective laser melting fabrication technique.

6 Summary and Outlook

For the first time, a large field of view (FoV) pixel super-resolution scanning transmission hard X-ray microscopy (PSR-STHXM) based on refractive multi-lenses (RMLs) was developed and demonstrated. The method takes advantage of specimen scanning through many identical and periodically spaced X-ray line or point foci, whereas the period is equal to one (or multiple) pixel size. Such a set-up reduces the scanning time drastically compared to already existing scanning microscopes.

The reason for this improvement consist, on one hand, in the development and fabrication of refractive multi-lens arrays with more than several hundred (1D lenses) up to several thousand (2D lenses) compound refractive lenses with distances in the range of 10 µm to 55 µm, on the other hand, in developing an algorithm that allows a pixel super-reconstruction of low pixel size recorded images at sub-pixel specimen position. This results in a spatial resolution equal to the diffraction-limited X-ray foci size (FWHM), which is defined by the lens's numerical aperture and could be below 1 µm depending on the design of the compound refractive lenses.

The PSR-STHXM required the development of specifically designed RMLs taking into account the synchrotron beamline characteristics and the corresponding X-ray detector constraints. To reach the final thesis goal, three successive X-ray optical elements, as the “heart” of PSR-STHXM, with each time innovation phases, were necessary:

1. 1D nickel refractive multi-lens (**RML**) for 17 keV
2. 2D SU-8 **CRML**s (compound refractive multi-lenses) for 34 keV.
3. **Staircase-array of inclined RMLs** for 35 keV.

They were designed and fabricated by pushing the limits of deep X-ray lithography and electroplating technique.

By tuning each step of the deep X-ray lithography and electroplating fabrication process, a 10 μm period single 1D nickel biconcave parabolic-shaped **RML** with the smallest radius of curvature (0.83 μm) was realized. The high quality of these fabricated structures allowed to achieve the 2 ± 0.06 μm diffraction-limited X-ray line foci width (FWHM) under monochromatic 17 keV X-rays illumination at the IMAGE beamline/KARA synchrotron facility. The spectral intensity enhancement (SIE) was 1.4 due to the high absorption of 8.5 μm web distance (distance between parabola apexes). However, all 250 individual lenses of the fabricated RML generated identical X-ray line foci with 10 μm spacing. This enabled us to perform the proof of concept of the PSR-STHXM using a detector with a pixel size seven times larger than the X-ray line foci width. By the PSR reconstruction of ten sub-pixel shifted LR images it was demonstrated that a spatial resolution of better than 1.5 μm can be achieved within a FOV of 2.5 mm × 60 μm [36]. The restriction of the horizontal direction to 60 μm is due to the height limit of the 1D lens. The exposure time was 10 s per image, resulting in the scanning time of about four minutes, which is only due to the relatively low photon flux at the IMAGE beamline. The image generation time can be significantly reduced by using 1D RML at the high brilliance synchrotron facilities like SPring-8.

The array of **2D CRMLs**, which was developed in this thesis, overcomes the limitations of 1D RMLs (high spatial resolution in one direction only). The fabricated 2D CRMLs consist of 34 × 34 1D RMLs connected in an interdigitated way and fixed with L-shaped mounting frames. Illuminated with 34 keV monochromatic X-rays, they generated 1156 point foci with an average size of 2 μm × 3.55 μm (vertically × horizontally). The spectral intensity enhancement was evaluated to be 16. Using the 2D CRMLs in a 2D PSR-STHXM and reconstructing the 2D PSR image from 110 images, a spatial resolution of $2 \times 2.5 \pm 0.9$ μm for the 55 μm pixel size was achieved within a FoV of 1.87×1.87 mm^2 [37]. The scanning time was only about four minutes.

To overcome the height limit of the X-ray RMLs and to increase the FoV also along the lens length to several centimeters, a concept of a **staircase-array of inclined RMLs** was turned into reality, and an array of RMLs was fabricated by tilted exposure deep X-ray lithography and electroplating [38]. When tilting the substrate against the X-ray beam appropriately, these RMLs creates a 2.5 cm (136±4 μm lens height × 189 RMLs) long line foci, resulting in a large FoV of 5 x 2.5cm^2. At the SPring- 8 / BL20B2 beamline using 35 keV X-rays, the 378000 individual line foci showed a 750 nm width. Imaging in a large FoV PSR-STHXM resulted in a 780 ± 40 nm spatial resolution in the scanning direction. The FoV of 1.64 × 1.64 cm^2 was not limited by the lens but by the detector area only; with this development, the FoV has been increased by more than one order of magnitude compared to the state of the art single probe STHXM and full-field TXM. It represents, actually, the largest FoV, which has been imaged, and only in a total image acquisition time of 4 minutes owing to the specimen scanning through 378000 X-ray line foci. Furthermore, compared to the standard X-ray radiography for the same FoV, the spatial resolution in the scanning direction was improved by a factor of 26.

The advantage of the large FoV PSR-STHXM was demonstrated by analyzing additively manufactured dental implant abutment made of titanium alloy. The image contrast and resolution were significantly improved compared to the standard X-ray radiography while keeping the FoV.

With the results presented in this thesis, the large FoV hard X-ray microscopy of extended and optically thick specimens with high resolution and fast image acquisition time has been successfully demonstrated. The FoV of the PSR-STHXM can be further increased by the fabrication of higher (up to 2 mm for SU-8 RMLs) inclined RMLs by further process optimization of deep X-ray lithography and electroplating. The development and realization of the 2D staircase array of inclined RMLs will improve the spatial resolution in two dimensions, resulting in a 2D PSR-STHXM with a cm range FoV. The development of a compound staircase array of inclined RMLs would enable

exploring PSR-STHXM for energies up to 100 keV, allowing the study of various samples for material science applications.

PSR-STXHM could be extended to multi-contrast imaging modality providing additional contrasts: phase and scattering [93]. In this case, each X-ray point foci should be centered in the border between four LR detector pixels (unit cell); line foci is in the border between two pixels, respectively. The detector should be placed behind the specimen at a distance equal to the focal distance. By placing the specimen in the focal distance and scanning it, the LR detector will record the changes in intensity, position, and size of X-ray foci in each unit cell according to the absorption, differential phase, and scattering. Consequently, it would be possible to reconstruct PSR multi-contrast images for multiple LR images with a high spatial resolution. This would allow to study weakly absorbing specimens as well as porous composite materials.

Furthermore, if the experiment focus concerns more the temporal resolution as the spatial one, the developed X-ray optics combined with high repetition rate X-ray detectors would enable to perform single-shot multimodal X-ray imaging giving the possibility to investigate dynamic processes [94][95]. Besides, the new optical elements could be used as a hard X-ray multi-lens interferometer for the wavefront investigations [50][51][96].

List of publications

Peer-reviewed publication list:

1. Mamyrbayev, T., Ikematsu, K., Meyer, P., Ershov, A., Momose, A., Mohr, J., "Super-resolution scanning transmission X-ray imaging using single biconcave parabolic refractive lens array", *Sci. Rep.* vol. 9 (2019)
2. Mamyrbayev, T.*, Opolka, A.*, Ershov, A., Gutekunst, J., Meyer, P., Ikematsu, K., Momose, A., Last, A. " Development of an array of compound refractive lenses for sub-pixel resolution, large field of view and time-saving in scanning hard X-ray microscopy", *Appl. Sci*. 10 (12) (2020)
3. Mamyrbayev, T., Ikematsu, K., Takano H., Wu, Y., Kimura, K., Doll, P., Last, A., Momose, A., and Meyer, P. "Staircase array of inclined refractive multi-lenses for a large field of view pixel super-resolution scanning transmission hard X-ray microscopy", *J. of Synchrotron. Rad.* (accepted on 09.02.2021)

Conferences (only as presenting author)

1. Mamyrbayev, T., Ikematsu, K., Meyer, P., Opolka, A., Last, A., Faisal, A., Farago, T., Kunka, D., Momose, A., and Mohr, J. " Improvement of spatial resolution in grating based X-ray interferometry", IMXP, Garmisch-Partenkirchen, Germany (2018) poster
2. Mamyrbayev, T., Ikematsu, K., Meyer, P., Zuber, M., Cecilia, A., Baumbach, T., Momose, A., and Mohr, J. "Fabrication of novel gratings to improve spatial resolution in X-ray phase imaging", XOPT, Yokohama, Japan (2018) oral talk
3. Mamyrbayev, T., Ikematsu, K., Meyer, P., Ershov, A., Cecilia, A., Bremer, S., Zuber, M., Momose, A., and Mohr, J. " Super-resolution scanning transmission X-ray imaging", XNPIG, Sendai, Japan (2019) poster

* Equally contributing authors

References

[1] H. Simons, A. King and W. Ludwig, "Dark-field X-ray microscopy for multiscale structural characterization," *Nat. Commun.,* vol. 6, pp. 6098, 2015.

[2] B. Larson, W. Yang and G. Ice. "Three-dimensional X-ray structural microscopy with submicrometre resolution," *Nature,* vol. 415, pp. 887–890, 2002.

[3] S. Di Fonzo, W. Jark and S. Lagomarsino, "Non-destructive determination of local strain with 100-nanometre spatial resolution," *Nature,* vol. 403, pp. 638–640, 2000.

[4] A. Sakdinawat and D. Attwood "Nanoscale X-ray imaging," *Nature Photon,* vol. 4, pp. 840–848, 2010.

[5] A. Koch, C. Raven, P. Spanne, and A. Snigirev, "X-ray imaging with submicrometer resolution employing transparent luminescent screens," *J. Opt. Soc. Am. A,* vol. 15, pp. 1940-1951, 1998.

[6] T. Martin and A. Koch, "Recent developments in X-ray imaging with micrometer spatial resolution." *J.Synchrotron Rad.,* vol. 13, pp. 180–194, 2006.

[7] P.A. Douissard, A. Cecilia, X. Rochet, X. Chapel, T. Martin, T. van de Kamp, L. Helfen, T. Baumbach, L. Luquot, X. Xiao, J. Meinhardt, A. Rack, "A versatile indirect detector design for hard X-ray microimaging." *JINST,* vol. 7, P09016–P09016, 2012. doi:10.1088/1748-0221/7/09/P09016

[8] W. Chao, B. Harteneck and J. Liddle, "Soft X-ray microscopy at a spatial resolution better than 15 nm," *Nature,* vol. 435, pp. 1210–1213, 2005.

[9] V. E. Cosslett, and W. C. Nixon, “X-ray shadow microscope,” *Nature* 168, pp. 436–438, 1951.

[10] P. Bleuet, et al., “A hard X-ray nanoprobe for scanning and projection nanotomography,” *Rev. Sci. Instrum.* 80, 056101, 2009.

[11] B. Niemann and D. Rudolph “X-ray microscopy with synchrotron radiation. *Appl. Opt.* 15, 1883–1884, 1976.

[12] J. C. Andrews, F. Meirer, Y. Liu, Z. Mester and P. Pianetta, “Transmission X-ray microscopy for full-field nano imaging of biomaterials,” *Microscopy research and technique*, vol. 74 no. 7, pp. 671–681, 2011.

[13] H. Simons, F. Stöhr, J. Michael-Lindhard, F. Jensen, O. Hansen, C. Detlefs and H. F. Poulsen “Full-field hard X-ray microscopy with interdigitated silicon lenses,” *Opt. Commun*., vol. 359, pp. 460–464, 2016.

[14] K. V. Falch, D. Casari, M. Di Michiel, C. Detlefs, A. Snigireva, I. Snigireva, V. Honkimäki and R. H. Mathiesen, “In situ hard X-ray transmission microscopy for material science,” *J. Mater. Sci.,* vol. 52, pp. 3497–3507, 2017.

[15] H. Rarback, et. al.“Scanning X-ray microscope with 75-nm resolution,” *Rev. Sci. Instrum.* 59, pp. 52–59, 1988.

[16] I. Mohacsi, I. Vartiainen and B. Rösner, “Interlaced zone plate optics for hard X-ray imaging in the 10 nm range,” *Sci. Rep.,* vol. 7, pp. 43624, 2017.

[17] H. Mimura, S. Handa, T. Kimura, H. Yumoto, D. Yamakawa, H. Yokoyama, S. Matsuyama, K. Inagaki, K. Yamamura, Y. Sano, K. Tamasaku, Y. Nishino, M. Yabashi, T. Ishikawa and K. Yamauchi, “Breaking the 10 nm barrier in hard-X ray focusing,” *Nat. Phys*., vol. 6, pp. 122–125, 2010.

[18] S. Matsuyama, S. Yasuda and J. Yamada, “50-nm-resolution full-field X-ray microscope without chromatic aberration using total-reflection imaging mirrors,” *Sci. Rep.,* vol. 7, pp. 46358, 2017.

[19] W. Luo, Y. Zhang, A. Feizi, Z. Göröcs and A. Ozcan, “Pixel super-resolution using wavelength scanning,” *Light Sci. Appl.,* vol. 5, e16060, 2016.

[20] W. Bishara, T. W. Su, A. F. Coskun, and A. Ozcan, “Lensfree on-chip microscopy over a wide field-of-view using pixel super-resolution,” *Opt. Express***,** vol. 18, pp. 11181–11191, 2010.

[21] S. C. Park, M. K. Park and M. G. Kang, "Super-resolution image reconstruction: a technical overview," *IEEE Signal Processing Magazine*, vol. 20, no. 3, pp. 21-36, 2003.

[22] J. Tian, K. Ma, “A survey on super-resolution imaging,” *SIViP*, vol. 5, pp. 329–342, 2011.

[23] S. Farsiu, M. D. Robinson, M. Elad and P. Milanfar, “Advances and challenges in super-resolution,” *Int. J. Imag. Syst. and Tech.,* vol. 14**,** pp. 47–57, 2004.

[24] M. C. Chiang and T. E. Boult, “Efficient super-resolution via image warping," *Image Vis. Comput.,* vol. 18, no. 10, pp. 761–771, 2000.

[25] S. Baker and T. Kanade, "Limits on super-resolution and how to break them," *IEEE Transactions on Pattern Analysis and Machine Intelligence*, vol. 24, no. 9, pp. 1167-1183, 2002.

[26] M. Irani and S. Peleg, “Improving resolution by image registration,” *CVGIP:Graph. Models Image Process*, vol. 53, pp. 231–239, 1991.

[27] N. Nguyen, P. Milanfar and G. Golub, "A computationally efficient superresolution image reconstruction algorithm," *IEEE Transactions on Image Processing*, vol. 10, no. 4, pp. 573-583, 2001.

[28] J. Yang, J. Wright, T. Huang and Yi Ma, "Image super-resolution as sparse representation of raw image patches," *2008 IEEE Conference*

on Computer Vision and Pattern Recognition, Anchorage, AK, pp. 1-8, 2008.

[29] S. Farsiu, M. D. Robinson, M. Elad and P. Milanfar, "Fast and robust multiframe super resolution," *IEEE Transactions on Image Processing*, vol. 13, no. 10, pp. 1327-1344, 2004.

[30] M. Viermetz, L. Birnbacher and M. Willner, “High resolution laboratory grating-based X-ray phase-contrast CT,” *Sci. Rep.*, vol.8, pp. 15884, 2018.

[31] S. Borman and R. Stevenson, “Spatial Resolution Enhancement of Low-Resolution Image Sequences A Comprehensive Review with Directions for Future Research,” Technical Report; Laboratory for Image and Signal Analysis (LISA), University of Notre Dame: Notre Dame, IN, USA, 1998.

[32] P. Vandewalle, S. Süsstrunk and M. Vetterli, “A frequency domain approach to registration of aliased images with application to super-resolution,” *EURASIP J. on Adv. In Signal Process (JASP)*, vol. 2006, no. 071459, pp. 1-14, 2006.
doi: https://doi.org/10.1155/ASP/2006/71459

[33] A. Lübcke, J. Braenzel, A. Dehlinger, M. Schnürer, H. Stiel, P. Guttmann, S. Rehbein, G. Schneider, S. Werner, R. Kemmler, S. Ritter, M. Raugust, T. Wende, M. Behrendt and M. Regehly, “Soft X-ray nanoscale imaging using a sub-pixel resolution charge coupled device (CCD) camera,” *Rev. Sci. Instrum.*, vol. 90, no. 043111, 2019.

[34] V. Nieuwenhove, J. Beenhouwer, F. Carlo, L. Mancini, F. Marone and J. Sijbers, “Dynamic intensity normalization using eigen flat fields in X-ray imaging,” *Opt. Express*, vol. 23, no. 21, pp. 27975-27989, 2015.

[35] S. Ehn, F. Epple, A. Fehringer, D. Pennicard, H. Graafsma, P. Noël and F. Pfeiffer, "X-ray deconvolution microscopy," *Biomed. Opt. Express,* vol. 7, pp. 1227-1239, 2016.

[36] T. Mamyrbayev, K. Ikematsu, P. Meyer, A. Ershov, A. Momose and J. Mohr, "Super-resolution scanning transmission X-ray imaging using single biconcave parabolic refractive lens array," *Sci. Rep.*, vol. 9, 14366, 2019.

[37] T. Mamyrbayev, A. Opolka, A. Ershov, J. Gutekunst, P. Meyer, K. Ikematsu, A. Momose and A. Last, "Development of an Array of Compound Refractive Lenses for Sub-Pixel Resolution, Large Field of View, and Time-Saving in Scanning Hard X-ray Microscopy," *Appl. Sci*., vol. 10, no. 12, pp. 4132, 2020.

[38] T. Mamyrbayev, K. Ikematsu, H. Takano, Y. Wu, K. Kimura, P. Doll, A. Last, A., Momose, and P. Meyer, "Staircase array of inclined refractive multi-lenses for a large field of view pixel super-resolution scanning transmission hard X-ray microscopy", *J. of Synchrotron. Rad.* (accepted on 09.02.2021)

[39] P. Meyer and J. Schulz, "Deep X-ray lithography. Chapter 16 in Micromanufacturing Engineering and Technology," ed. Y. Qin, 2nd ed., Elsevier Inc., Boston, Massachusetts, pp. 365–391, 2015.

[40] A. Last, and J. Mohr, Fehllicht in LIGA-Mikrospektrometern, Forschungszentrum Karlsruhe GmbH, scientific report no. FZKA-6585, ISSN 0947-8620, 2003, doi: 10.5445/IR/3402003.

[41] W. C. Röntgen, „Über eine neue Art von Strahlen. (Vorläufige Mitteilung)", *Sitzungsberichte der Würzburger Phys.-Medic. Gesellschaft*, 1896.

[42] J. Als-Nielsen and D. McMorrow, "Elements of Modern X-Ray Physics", 2nd ed., John Wiley & Sons, Wiley: West Sussex, UK, 2011.

[43] P. Kirkpatrick and A. V. Baez, “Formation of optical images by X-rays,” *J. Opt. Soc. Am*., vol. 38, pp. 766–774, 1948.

[44] H. Mimura, S. Morita, T. Kimura, D. Yamakawa, W. Lin, Y. Uehara, S. Matsuyama, H. Yumoto, H. Ohashi, K. Tamasaku, Y. Nishino, M. Yabashi, T. Ishikawa, H. Ohmori and K. Yamauchi, “Focusing mirror for X-ray free-electron lasers,” *Rev. Sci. Instrum.,* vol. 79, 083104, 2008.

[45] S. Matsuyama, Y. Emi, H. Kino, Y. Kohmura, M. Yabashi, T. Ishikawa and K. Yamauchi, “Achromatic and high-resolution full-field X-ray microscopy based on total-reflection mirrors,” *Opt. Express*, vol. 23, no. 8, pp. 9746–9752, 2015.

[46] J. Vila-Comamala, S. Gorelick, E. Färm, C. M. Kewish, A. Diaz, R. Barrett, V. A. Guzenko, M. Ritala and C. David, “Ultra-high resolution zone-doubled diffractive X-ray optics for the multi-kev regime,” *Opt. Express*, vol. 19, no. 1, pp. 175–184, 2011.

[47] S. Bajt, M. Prasciolu, H. Fleckenstein, M. Domaracký, H. Chapman, A. Morgan, O. Yefanov, M. Messerschmidt, Y. Du, K. Murray, V. Mariani, M. Kuhn, S. Aplin, K. Pande, P. Villanueva-Perez, K. Stachnik, J. Chen, A. Andrejczuk, A. Meents, A. Burkhardt, D. Pennicard, X. Huang, H. Yan, E. Nazaretski, Y. Chu and C. Hamm, “X-ray focusing with efficient high-NA multilayer Laue lenses,” *Light: Sci. Appl*., vol.7, pp. 17162, 2018.

[48] A. Snigirev, V. Kohn, I. Snigireva und B. Lengeler, “A compound refractive lens for focusing high-energy X-rays,” *Nature*, vol. 384 pp. 49-51, 1996.

[49] C. G. Schroer, T. F. Günzler, B. Benner, M. Kuhlmann, J. Tümmler, B. Lengeler, C. Rau, T. Weitkamp, A. Snigirev and I.Snigireva, “Hard X-ray full field microscopy and magnifying microtomography using compound refractive lenses,” *Nuclear Instruments and Methods in Physics Research Section A: Accelerators, Spectrometers,*

Detectors and Associated Equipment, vol. 467–468, no. 2, pp. 966-969, 2001.

[50] A. Snigirev, I. Snigireva, M. Lyubomirskiy, V. Kohn, V. Yunkin and S. Kuznetsov, "X-ray multilens interferometer based on Si refractive lenses," *Opt. Express*, vol. 22, no. 21, pp. 25842–25852, 2014.

[51] M. Lyubomirskiy, I. Snigireva, V. Kohn, S. Kuznetsov, V. Yunkin, G. Vaughan and A. Snigirev, "30-Lens interferometer for high-energy X-rays," *J. Synchrotron Rad.*, vol. 23, no. 5, pp. 1-6, 2016.

[52] T. dos Santos Rolo, S. Reich, D. Karpov, S. Gasilov, D. Kunka, E. Fohtung, T. Baumbach and A. Plech, "A Shack-Hartmann sensor for single-shot multi-contrast imaging with hard X-rays," *Appl. Sciences*, vol. 8, no. 5, pp. 737-749, 2018.

[53] A. Mikhaylov, S. Reich, A. Plech, M. Zakharova, V. Vlnieska and D. Kunka, "2D lens array for multi-contrast X-ray imaging," *Proc. SPIE*, vol. 11032, SPIE Optics + Optoelectronics, Prague, Czech Republic, p. 1103208, 2019.
doi: https://doi.org/10.1117/12.2520687

[54] A. Mikhaylov, S. Reich, M. Zakharova, V. Vlnieska, R. Laptev, A. Plech and D. Kunka, "Shack–Hartmann wavefront sensors based on 2D refractive lens arrays and super-resolution multi-contrast X-ray imaging," *J. Synchrotron Rad.*, vol. 27, pp. 788-795, 2020.

[55] S. Reich, T. dos Santos Rolo, A. Letzel, T. Baumbach and A. Plech, "Scalable, large area compound array refractive lens for hard X-rays," *Appl. Phys. Lett.*, vol. 112, no. 15, pp. 151903, 2018.

[56] R. W. James and W. L. Bragg, "The optical principles of the diffraction of X-rays," G. Bell & Sons, London, UK, 1962.

[57] E. Hecht, "Optics," 4th Edition, Addison Wesley, San Francisco, USA, 2001.

[58] B. Lengerer and J. Tümmler, “Transmission and gain of singly and doubly focusing refractive X-ray lenses,” *J. of Applied Phys*., vol. 84, pp. 5855-5861. 1998.

[59] B. Lengeler, C. G. Schroer, B. Benner, A. Gerhardus, T. F. Günzler, M. Kuhlmann, J. Meyer and C. Zimprich, “Parabolic refractive lenses,” *J. Synchrotron Rad*., vol. 9, pp. 119-124, 2002.

[60] N. R. Pereira, E. M. Dufresne, R. Clarke and D. A. Arms, “Parabolic lithium refractive optics for x rays,” *Review of Scientific Instruments,* vol. 75, pp. 37, 2004.

[61] K. Young, A. Khounsary, A. N. Jansen, E. M. Dufresne and P. Nash, “Fabrication and Performance of a Lithium X-Ray Lens,” *AIP Conference Proceedings,* vol. 879, Melville, New York: American Institute of Physics, USA, pp. 989-993, 2007.
doi: https://doi.org/10.1063/1.2436228

[62] D. V. Byelov, J. M. Meijer, I. Snigireva, A. Snigirev, L. Rossi, E. van den Pol, A. Kuijk, A. Philipse, A. Imhof, A. van Blaaderen, G. J. Vroege and A. V. Petukhov, “In situ hard X-ray microscopy of self-assembly in colloidal suspensions,” *RSC Adv.*, vol. 3, pp. 15670-15677, 2013.

[63] C. G. Schroer, M. Kuhlmann, B. Lengeler, T. F. Günzler, O. Kurapova, B. Benner, C. Rau, A. S. Simionovici, A. Snigirev and I. Snigireva, “Beryllium parabolic refractive x-ray lenses,” *Proc. SPIE*, vol. 4783, International Symposium on Optical Science and Technology, Seattle, WA, USA, pp. 10-19, 2002.
doi: https://doi.org/10.1117/12.451013

[64] B. Lengeler, C. G. Schroer, M. Kuhlmann, B. Benner, T. F. Günzler, O. Kurapova, A. Somogyi, A. Snigirev and I. Snigireva, “Beryllium parabolic refractive x-ray lenses,” *AIP Conference Proceedings,* vol. 705, Melville, New York: American Institute of Physics, USA, pp. 748-751, 2004. doi: https://doi.org/10.1063/1.1757904

[65] A. Stein, K. Evans-Lutterodt, N. Bozovic and A. Taylor, “Fabrication of silicon kinoform lenses for hard x-ray focusing by electron beam lithography and deep reactive ion etching,” *J. Vac. Sci. Technol. B*, vol. 26 no. 1, pp. 122-127, 2008.

[66] L. Alianelli, I. Pape, J. P. Sutter, O. J. L. Fox, K. J. S. Sawhney and K. Korwin-Mikke, “Aberration-free x-ray lenses made of silicon,” *Proc. SPIE*, vol. 9963, SPIE Optical engineering + Applications, San Diego, California, USA, 2016.
doi: https://doi.org/10.1117/12.2240005

[67] E. Reznikova, T. Weitkamp, V. Nazmov, M. Simon, A. Last and V. Saile, “Transmission hard x-ray microscope with increased view field using planar refractive objectives and condensers made of SU-8 polymer,” *J. Phys.: Conf. Ser.*, vol. 186, 012070, 2009.

[68] F. Marschall, A. Last, M. Simon, H. Vogt and J. Mohr, "Simulation of aperture-optimised refractive lenses for hard X-ray full field microscopy," *Opt. Express*, vol. 24, pp. 10880-10889, 2016.

[69] B. Nöhammer, C. David, H. Rothuizen, J. Hoszowska and A. Simionovici, “Deep reactive ion etching of silicon and diamond for the fabrication of planar refractive hard x-ray lenses,” *Microelectron Eng.*, vol. 67–68, pp. 453–460, 2003.

[70] P. Medvedskaya, I. Lyatun, S. Shevyrtalov, M. Polikarpov, I. Snigireva, V. Yunkin and A. Snigirev, "Diamond refractive micro-lenses for full-field X-ray imaging and microscopy produced with ion beam lithography," *Opt. Express*, vol. 28, no. 4, pp. 4773-4785, 2020.

[71] A. Snigirev, I. Snigireva, M. Michiel, V. Honkimaki, M. Grigoriev,V. Nazmov, E. Reznikova, J. Mohr and V. Saile, "Submicron focusing of high-energy X-rays with Ni refractive lenses," *Proc. SPIE*, vol. 5539, Optical Science and Technology, the SPIE 49th Annual Meeting, 2004, Denver, Colorado, USA pp. 244-250, 2004. doi: https://doi.org/10.1117/12.564545

[72] V. Nazmov, E. Reznikova, A. Last, J. Mohr, V. Saile, M. Di Michiel and J. Göttert, “Crossed planar x-ray lenses made from nickel for x-ray micro focusing and imaging applications,” *Nucl. Instrum. Methods Phys. Res. A,* vol. 582, no. 1, pp. 120–122, 2007.

[73] B. Lengeler, C. Schroer, J. Tümmler, B. Benner, M. Richwin, A. Snigirev, I. Snigireva and M. Drakopoulos, “Imaging by parabolic refractive lenses in the hard X-ray range,” *J. Synchrotron Rad.*, vol. 6, no. 6, pp. 1153–1167, 1999.

[74] V. G. Kohn, I. Snigireva und A. Snigirev, “Diffraction theory of imaging with X-ray compound refractive lens,” *Optics Communications*, vol.216, no. 4-6, pp. 247-260, 2003.

[75] V. G. Kohn, “Effective aperture of X-ray compound refractive lenses,” *J. Synchrotron Rad.*, vol. 24, pp. 609-614, 2017.

[76] J. T. Cremer, “Advances in imaging and electron physics,” vol. 172, Part 1: Neutron and X-ray microscopy, 1st edition, Elsevier/Academic Press, Amsterdam, the Netherlands, 2012.

[77] S. G. Lipson, D. S. Tannhauser and H. S. Lipson, “Optical Physics,” 3rd edition, Cambridge University Press, Cambridge, UK, 1995.

[78] A. K. Petrov, V. O. Bessonov, K. A. Abrashitova, N. G. Kokareva, K. R. Safronov, A. A. Barannikov, P. A. Ershov, N. B. Klimova, I. I. Lyatun, V. A. Yunkin, M. Polikarpov, I. Snigireva, A. A. Fedyanin, and A. Snigirev, “Polymer X-ray refractive nano-lenses fabricated by additive technology,” *Opt. Express*, vol. 25, no. 25, pp. 14173, 2017.

[79] V. Nazmov, E. Reznikova, A. Snigirev, I. Snigireva, M. DiMichiel, M. Grigoriev, J. Mohr, B. Matthis und V. Saile, “LIGA fabrication of X-ray Nickel lenses,” *Microsystem Technologies,* vol. 11, pp. 292–297, 2005.

[80] V. Nazmov, J. Mohr, H. Vogt, R. Simon and S. Diabaté “Multi-field X-ray microscope based on array of refractive lenses,” *J. Micromech. Microeng.*, vol. 24, no. 7, 2014.

[81] V. Nazmov, E. Reznikova, J. Mohr, V. Saile, L. Vincze, B. Vekemans, S. Bohic and A. Somogyi, “Parabolic crossed planar polymeric X-ray lenses,” *J. Micromech. Microeng.*, vol. 21, no. 1, 2011.

[82] C. Krywka, A. Last, F. Marschall, O. Márkus, S. Georgi, M. Müller and J. Mohr, “Polymer compound refractive lenses for hard X-ray nanofocusing,” *AIP Conference Proceedings*, vol. 1764, Melville, New York: American Institute of Physics, USA, p. 02001, 2016. doi: https://doi.org/10.1063/1.4961129

[83] V. Nazmov, E. Reznikova, J. Mohr, A. Snigirev, I. Snigireva, S. Achenbach and V. Saile, “Fabrication and preliminary testing of X-ray lenses in thick SU-8 resist layers,” *Microsystem Technologies*, vol.10, pp. 716–721, 2004.

[84] E. Kornemann, O. Márkus, A. Opolka, T. Zhou, I. Greving, M. Storm, C. Krywka, A. Last and J. Mohr, "Miniaturized compound refractive X-ray zoom lens," *Opt. Express*, vol. 25, no. 19, pp. 22455-22466, 2017.

[85] R. Ballabriga, J. Alozy, G. Blaj, M. Campbell, M. Fiederle, E. Frojdh, E. H. M. Heijne, X. Llopart, M. Pichotka, S. Procz, L. Tlustos and W. Wong, “The MEDIPIX3RX: a high resolution, zero dead-time pixel detector readout chip allowing spectroscopic imaging,” *J. Instrum.*, vol. 8, C02016, 2013.

[86] E. Kornemann, T. Zhou, O. Márkus, A. Opolka, T. U. Schuelli, J. Mohr and A. Last, “X-ray zoom lens allows for energy scans in X-ray microscopy,” *Opt. Express*, vol**.** 27, no. 1, pp. 185-195, 2019.

[87] E. Gullikson, Index of refraction. Last access date: 12.10.2020 doi: http://henke.lbl.gov/optical_constants/getdb2.html

[88] VDI/VDE 5575 part1:2007-12 X-ray optical systems; terms and definition. Berlin, Beuth Verlag, 2017.

[89] W. Jark, A. Opolka, A. Cecilia and A. Last, “Zooming X-rays with a single rotation in X-ray prism zoom lenses (XPZL),” *Opt. Express*, vol. 27, no. 12, pp. 16781-16790, 2019.

[90] R. J. Marks II, “Introduction to Shannon Sampling and Interpolation Theory,” Springer-Verlag, New York, USA, 1991.

[91] C. S. Wu, Y. Makiuchi and C. D. Chen, “High-energy Electron Beam Lithography for Nanoscale Fabrication,” in Lithography, ed. by M. Wang, InTech, Rijeka, Croatia, p. 241, 2010.

[92] T. Vilaro, C. Colin and J. D. Bartout, “As-fabricated and heat-treated microstructures of the Ti-6Al-4V alloy processed by selective laser melting,” *Metall. Mater. Trans. A.*, vol. 42, pp. 3190–3199, 2011.

[93] K. R. Rix, T. Dreier, T. Shen and M. Bech, “Super-resolution X-ray phase-contrast and dark-field imaging with a single 2D grating and electromagnetic source stepping,” *Phys. Med. Biol.*, vol. 64, no. 16, pp. 165009, 2019.

[94] S. C. Mayo and B. Sexton, “Refractive microlens array for wave-front analysis in the medium to hard X-ray range,” *Opt. Lett.*, vol. *29*, no. 8, pp. 866-868, 2004.

[95] A. Letzel, S. Reich, T. dos Santos Rolo, A. Kanitz, J. Hoppius, A. Rack, M. Olbinado, A. Ostendorf, B. Gökce, A. Plech and S. Barcikowski, “Time and Mechanism of Nanoparticle Functionalization by Macromolecular Ligands during Pulsed Laser Ablation in Liquids,” *Langmuir*, vol. 35, no. 8, pp. 3038-3047, 2019.

[96] D. Zverev, I. Snigireva, V. Kohn, S. Kuznetsov, V. Yunkin and A. Snigirev, "X-ray phase-sensitive imaging using a bilens interferometer based on refractive optics," *Opt. Express*, vol. 28, no. 15, pp. 21856-21868, 2020